Morschhauser, A., Lesur, V., Grott, M. (2014): A spherical harmonic model of the lithospheric magnetic field of Mars. - *Journal of Geophysical Research*, *119*, 6, p. 1162-1188.

DOI: http://doi.org/10.1002/2013JE004555

AGU PUBLICATIONS

JGR

Journal of Geophysical Research: Planets

RESEARCH ARTICLE

10.1002/2013JE004555

Key Points:
- SH model up to degree and order 110 of the magnetic lithospheric field of Mars
- Several techniques have been used to obtain a stable and well-resolved model
- Anomalies over small craters, volcanoes, and isolated anomalies are described

Supporting Information:
- Readme
- Figure S1
- Figure S2
- Figure S3
- Figure S4
- Figure S5
- Figure S6
- Figure S7
- Figure S8
- Figure S9
- Table S1
- Table S2
- Table S3
- Table S4
- Table S5
- Table S6

Correspondence to:
A. Morschhauser,
achim.morschhauser@dlr.de

Citation:
Morschhauser, A., V. Lesur, and M. Grott (2014), A spherical harmonic model of the lithospheric magnetic field of Mars, *J. Geophys. Res. Planets*, *119*, 1162–1188, doi:10.1002/2013JE004555.

Received 11 OCT 2013
Accepted 22 APR 2014
Accepted article online 28 APR 2014
Published online 9 JUN 2014

A spherical harmonic model of the lithospheric magnetic field of Mars

A. Morschhauser[1], V. Lesur[2], and M. Grott[1]

[1]Department of Planetary Physics, German Aerospace Center, Berlin, Germany, [2]Department of Geophysics, German Research Center for Geosciences, Potsdam, Germany

Abstract We present a model of the lithospheric magnetic field of Mars which is based on Mars Global Surveyor orbiting satellite data and represented by an expansion of spherical harmonic (SH) functions up to degree and order 110. Several techniques were applied in order to obtain a reliable and well-resolved model of the Martian lithospheric magnetic field: A modified Huber-Norm was used to properly treat data outliers, the mapping phase orbit data was weighted based on an a priori analysis of the data, and static external fields were treated by a joint inversion of external and internal fields. Further, temporal variabilities in the data which lead to unrealistically strong anomalies were considered as noise and handled by additionally minimizing a measure of the horizontal gradient of the vertically down internal field component at surface altitude. Here we use an iteratively reweighted least squares algorithm to approach an absolute measure (L1 norm), allowing for a better representation of strong localized magnetic anomalies as compared to the conventional least squares measure (L2 norm). The resulting model reproduces all known characteristics of the Martian lithospheric field and shows a rich level of detail. It is characterized by a low level of noise and robust when downward continued to the surface. We show how these properties can help to improve the knowledge of the Martian past and present magnetic field by investigating magnetic signatures associated with impacts and volcanoes. Additionally, we present some previously undescribed isolated anomalies, which can be used to determine paleopole positions and magnetization strengths.

1. Introduction

The Mars Global Surveyor (MGS) spacecraft operated from 1997 to 2006 in Martian orbit and was the first mission to provide magnetic field measurements of Mars at a sufficiently low altitude to reveal the characteristics of the Martian magnetic field. The early mission phases include the aerobraking and science phase orbits (AB/SPO), which are characterized by strongly varying altitudes. At altitudes below 200 km, these early mission phases provide mainly dayside data with sparse global coverage [*Acuña et al.*, 1999]. They are complemented by the later mapping phase orbit (MPO) data, which provide dense global coverage during day- and nighttime at a nearly constant altitude of around 400 km.

Earliest results based on AB/SPO data already indicated that Mars does not possess a relevant large-scale magnetic field originating in an active core dynamo but rather relatively strong small-scale magnetic sources most probably originating in the lithosphere [*Acuña et al.*, 1998; *Purucker et al.*, 2000]. The strongest magnetic fields are observed over the southern highlands, mostly in Terra Sirenum and Terra Cimmeria between 120°E and 210°E [*Acuña et al.*, 1999], which are situated in ancient, mostly Noachian terrain. Their magnetic field signature is ~10 times stronger than lithospheric anomalies usually encountered on Earth [*Connerney et al.*, 1999; *Purucker et al.*, 2000; *Voorhies et al.*, 2002], implying either large volumes of magnetized material, very strong remanence, or both [*Connerney et al.*, 1999]. The northern lowlands, on the other hand, are thought to be only weakly magnetized, with the exception of some magnetic anomalies near the north pole [*Acuña et al.*, 1999; *Hood and Zakharian*, 2001].

Although much information can be extracted from the raw data, several problems arise when a more accurate description of the lithospheric magnetic field is necessary. First, the raw data generally contain field contributions of non-lithospheric origin [*Acuña et al.*, 1999; *Ferguson et al.*, 2005]. Furthermore, each datum is associated with signals generated over a relatively large area of magnetized rock, as the footprint of the data points approximately corresponds to the satellite altitude. Another difficulty arises from the fact that the data were obtained at varying altitudes. Lithospheric field models are a valuable tool to address these problems, as they enable a consistent projection and downward continuation to any altitude within the

error limits of the data. Also, they provide a mathematical way to separate the internal and external parts of the field relative to the satellite's altitude and to reduce the leakage of nonlithospheric field contributions into the lithospheric field model.

Published models of the lithospheric remanent field can be grouped according to the underlying data set and the chosen representation of the lithospheric field. The first published model [*Purucker et al.*, 2000] is based on binned AB/SPO data and describes the radial magnetic field component using 11,550 radially oriented equivalent source dipoles located on the mean surface of Mars (mean dipole spacing 111 km). This model was later improved by *Langlais et al.* [2004], who used a combination of AB/SPO and MPO data and all three vector components of the magnetic field in order to simultaneously solve for the directions and magnetizations of 4840 dipoles located 20 km below the mean surface altitude (mean dipole spacing 173 km). Using the same approach, *Langlais et al.* [2010] presented a new model based on more measurements, including Electron Reflectometry (ER) data [*Lillis et al.*, 2008a], sorted with an improved data selection scheme and an increased mesh resolution (dipole spacing close to 130 km). Furthermore, *Whaler and Purucker* [2005] presented a continuous magnetization model which does not depend on the resolution of the dipole grid. However, it is based on the AB/SPO/MPO data set of *Cain et al.* [2003], thus not containing any data beyond 2003. Using the same data set, *Chiao et al.* [2006] derived another equivalent source dipole model implementing a wavelet transform which allows for independently regularizing different spatial wavelengths. These lithospheric models have in common that they directly solve for a rock magnetization distribution describing the field measurements. However, it should be pointed out that without additional information an infinite number of magnetization solutions correctly describe the data [*Runcorn*, 1975; *Parker et al.*, 1987; *Lesur and Jackson*, 2000; *Gubbins et al.*, 2011]. Such additional information could be the assumption that no magnetic annihilators are present and to additionally minimize the root-mean-square magnetization amplitude [*Whaler and Purucker*, 2005; *Langlais et al.*, 2004].

A different approach consists of using spherical harmonic functions to describe the potential associated with the magnetic field. In this case, information on magnetization is only indirectly obtained, but both representations can be transformed into each other [*Arkani-Hamed*, 2002a; *Lesur*, 2006]. A first spherical harmonic model up to degree and order 50 was proposed by *Arkani-Hamed* [2001a] who used all three vector components of the AB/SPO mission phases. This model was later improved by including MPO data [*Arkani-Hamed*, 2002b]. A spherical harmonic model up to degree and order 90 was compiled by *Cain et al.* [2003], who filled the gaps of the AB/SPO data set with MPO data and used all three vector components. The latest spherical harmonic model is expanded up to degree and order 62 and was derived on the basis of two temporally separated MPO data sets using covariance analysis and the radial field component only, as this component is least contaminated by external fields [*Arkani-Hamed*, 2004a]. Finally, a combined approach was used by *Lillis et al.* [2010], who first used equivalent source dipoles to remove external fields by fitting adjacent tracks, and subsequently converted this solution to a spherical harmonic model.

Using these models, much has been learned about the history of the Martian lithospheric magnetic field, but many details remain disputed. In particular, there exist several hypotheses of when the core dynamo shut down. An early cessation of the dynamo is suggested by the apparently demagnetized major impact basins such as Hellas, Isidis, Argyre, and Utopia [*Acuña et al.*, 1999; *Mohit and Arkani-Hamed*, 2004; *Lillis et al.*, 2008b] or the lack of magnetization over the large volcanic provinces of Tharsis and Elysium [*Acuña et al.*, 1999; *Arkani-Hamed*, 2004b; *Johnson and Phillips*, 2005]. On the other hand, the strongest magnetic fields above regions of Noachian and Hesperian crust are similar in strength [*Milbury and Schubert*, 2010] and modeled paleopoles have been found to cluster near the geographic poles, when Hesperian-aged crust is overlying the respective magnetic anomaly, whereas older crust is correlated with paleopoles near the geographic equator [*Milbury et al.*, 2012]. These observations support the hypothesis of a late dynamo shutdown in the Hesperian. In addition, the dynamo may have started only after the formation of Tharsis and the large impact basins [*Schubert et al.*, 2000]. In any case, a late dynamo shutdown is compatible with positive magnetic anomalies associated with volcanic edifices younger than the major impact basins [*Lillis et al.*, 2006; *Langlais and Purucker*, 2007; *Hood et al.*, 2010]. However, it has been pointed out that the interpretation of the magnetization of volcanic features can be ambiguous [*Lillis et al.*, 2006] and the surface age might not be representative for the time of (de)magnetization [*Johnson and Phillips*, 2005]. Also, the dynamo may have started before the primordial crust had formed and cooled [*Stevenson*, 2001], or up to 100 Myr later, as there are large regions with no detectable fields over old terrains [*Arkani-Hamed and Boutin*, 2012]. Another unresolved question is the location of paleopoles, which contain information about the

dynamics of the ancient core dynamo as well as true polar wander. The paleopole positions calculated by various investigators are scattered over all latitudes (for an overview see *Milbury and Schubert* [2010]), but little information on the robustness of the results is given. The origin of the observed large contrasts of measured magnetic fields is also debated, and prominent features include large low-field regions over parts of the Noachian crust and in the northern lowlands as well as the concentration of the strongest magnetic fields in Terra Sirenum and Terra Cimmeria. Possible explanations for the observed large contrasts of lithospheric fields include a hemispherical dynamo [*Stanley et al.*, 2008; *Amit et al.*, 2011; *Dietrich and Wicht*, 2013], with the caveat that such a dynamo may lead to fast magnetic pole reversals on the order of 10 kyr and fail to explain the observed overall magnetization [*Dietrich and Wicht*, 2013]. An asymmetric degree-one convection pattern in the mantle could also be responsible for the formation of the topographic and magnetic dichotomy, either due to the concentration of melt production in one hemisphere [*Citron and Zhong*, 2012] or due to thermal conditions leading to mineral phase transformations, e.g., the formation of serpentine [*Quesnel et al.*, 2009; *Chassefière et al.*, 2013]. Also, a late start of the dynamo and subsequent localized magnetization by magmatic intrusions has been suggested [*Arkani-Hamed and Boutin*, 2012], which could have been locally favored by chemical alterations, caused by, e.g., elevated oxygen fugacity and the presence of water in the crust [*Hood et al.*, 2010]. Alternatively, the lowlands formation process could have erased any previous magnetization [*Arkani-Hamed*, 2004b].

Here we present a model of the lithospheric magnetic field of Mars represented by an expansion of spherical harmonic functions up to degree and order 110. Due to its higher resolution and its robustness when downward continued to lower altitudes, this model will help to address some of the open questions mentioned above. We will present examples of how this can be achieved and highlight some magnetic anomalies visible in the resulting field map, but a detailed study to investigate the above questions is beyond the scope of this paper. The presented model is based on the entire MGS magnetometer data set, including MPO and AB/SPO data. Several techniques have been applied in order to obtain a reliable and well-resolved model of the Martian lithospheric magnetic field. These include a joint inversion of internal and external fields, a data-based determination of a priori MPO data weights, a regularization scheme to minimize the influence of nonlithospheric fields which allows for sharp field gradients, and a statistical treatment of data outliers.

These techniques and the detailed process of deriving the presented lithospheric magnetic field model will be discussed in the following sections and are schematically illustrated in Figure 1. The red part of this figure shows the used data set including the applied selection criteria, which will be described in section 2. The remaining part of Figure 1 should be read from top to bottom and describes a number of preliminary models, indicated by gray trapezoids, with subsequent models containing all of the features of their predecessors. These intermediate models have been calculated either to obtain statistical values of the residuals between the data and the model, or to investigate some basic model parameters whenever the usage of a more complex model would have consumed considerably more computational power without significantly changing the results. An example for the former is the determination of the AB/SPO data weights (W-model in the dark blue box), whereas the determination of the damping parameter (L2 model in the orange box) and maximum spherical harmonic degree ($ABSPO_{Lint}$-models in the light blue box) are examples of the latter.

The mathematical description of the applied data inversion techniques including regularization and model parameterization will be discussed in section 3. Results in terms of a global map and a statistical assessment of the data fit will be presented in section 4. In this section, we will also investigate the effectiveness of the applied regularization technique and give some examples of how the presented model can help to improve our knowledge of the past and present Martian magnetic field. Finally, we will conclude the paper in section 5 by summarizing the strengths and weaknesses of the presented model.

2. Data and Estimation of Their Errors

We use vector magnetic field data as measured by the two fluxgate magnetometers on board the Mars Global Surveyor (MGS) spacecraft, which operated for almost a decade (1997–2006) in Martian orbit. The spacecraft initially entered into a highly elliptical orbit with a low periapsis (~100 km). This initial phase was used to slow the spacecraft with the help of atmospheric drag and is therefore called the aerobraking (AB1) phase. It was followed by the science phase orbit (SPO), which was used to adjust the phasing of the orbit with respect to local time entry, and a second aerobraking phase (AB2) with similar orbit parameters as AB1.

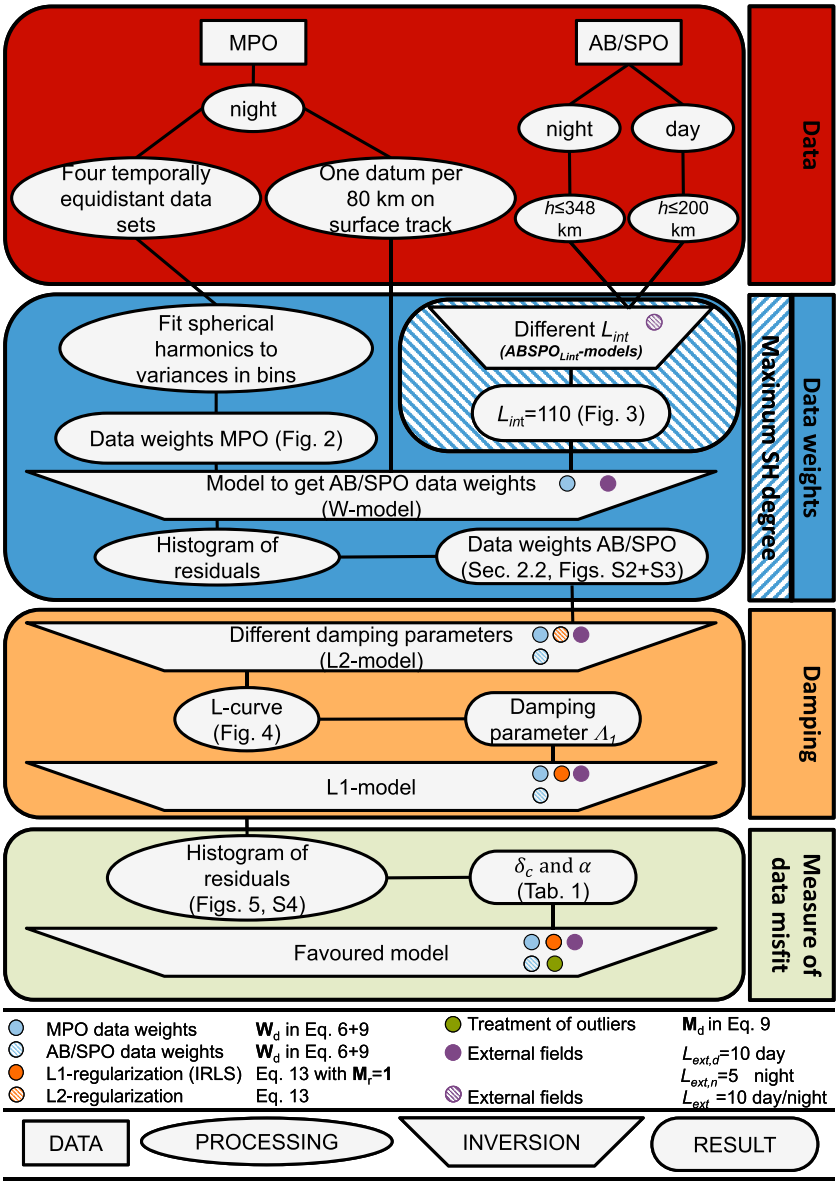

Figure 1. Schematic illustration of the steps involved in deriving the presented lithospheric field model with a description of the meaning of the symbols in the lowest part of the figure. The altitude above the mean radius of Mars is given by h, and L_{int}, $L_{ext,d}$ and $L_{ext,n}$ are the internal, dayside external, and nightside external maximum degree and order of the spherical harmonic expansion, respectively. $\mathbf{W}_d$ is the data weight matrix, $\mathbf{M}_d$ is the data misfit matrix (cf. equations (6), (9), and (14)), and δ_c and α are parameters of the assumed error probability density function (cf. equation (8)). The figure should be read from top to bottom and subsequent models contain all of the features of their predecessors. The red area illustrates the initial data selection as described in section 2. Both mapping phase orbit (MPO) and aerobraking with science phase orbit (AB/SPO) data are used and processed differently. The blue area describes the selection of data weights (dark blue) and the maximum spherical harmonic degree (light blue) and the orange area shows how the damping parameter is determined. Finally, the green area describes the introduction of an appropriate norm for treating data outliers and how the final model is obtained.

Eventually, MGS reached its final mapping phase orbit (MPO) in March 1999. This orbit was Sun-synchronous, passing the equator at 2 A.M./2 P.M. local time, had a nearly polar inclination of $i = 92.96°$, and was almost circular with altitudes ranging from 368 to 438 km above the surface of Mars [*Albee et al.*, 2001].

The fluxgate magnetometers on board MGS were attached to the edges of the solar panels, such that disturbances from the spacecraft field were minimized. They provided fast vector measurements with up to 32 samples/s [*Acuña et al.*, 2001]. These samples were averaged on the spacecraft and 12 bit values were

transmitted every 0.75, 1.50, and 3.00 s, depending on telemetry rate. Magnetometer data are available for all mission phases and have been corrected for variable and static spacecraft-generated fields through a variety of calibration tests and by comparing the output of the two magnetometers [*Acuña et al.*, 2001]. The data are provided in a Cartesian, planetocentric, as well as in a Cartesian, Sun-related coordinate system. The first system was used to transform the data into a spherical planetocentric coordinate system, where the magnetic field is expressed in terms of the components pointing horizontally north (X), east (Y), and vertically down (Z). The Sun-related system and the solar panel currents were used to identify if the data were collected at dayside or nightside.

In addition to the fluxgate magnetometers, MGS was equipped with an Electron Reflectometer (ER), which measures the energy and angular distributions of 10 eV to 20 keV electrons [*Mitchell et al.*, 2001]. In combination with the measured vector magnetic field at orbit altitude, this can be used to remotely measure the magnetic field intensity at the altitude where electrons are absorbed in the Martian atmosphere [*Lillis et al.*, 2008c]. On Mars, this altitude corresponds to approximately 170–185 km above the surface [*Lillis et al.*, 2004, 2008c]. The Electron Reflectometer operated during the entire mapping phase (MPO), but not through all of the earlier mission phases (AB/SPO), due to concerns about high-voltage arcing in the dense atmosphere (R. Lillis, personal communication, 2014). The most recent ER map, based on binned and averaged measurements of the mapping phase (MPO), was released by *Lillis et al.* [2008a]. We will use this data to validate some predictions of the presented model (cf. Figures 10 and 14).

As will be described below, the AB/SPO and MPO data sets have complementary strengths and weaknesses, and it is necessary to combine the lowest altitude AB/SPO data with the MPO data in order to obtain dense global coverage and the best possible resolution for lithospheric magnetic field models [*Arkani-Hamed*, 2002b; *Cain et al.*, 2003; *Langlais et al.*, 2004].

In addition to the characteristics of these data sets, we will present a procedure to estimate data weights for each data set. Data weights should ideally represent the variance of the data errors when inverting under the assumption of normally distributed errors (cf. section 3.2). However, they are difficult to assess a priori, as detailed knowledge of possible error sources would be necessary. For the MPO data, we estimated spatially resolved variances from the data itself, whereas for the AB/SPO data, we estimated the variance for each vector component from the residuals of the AB/SPO data to a preliminary model (cf. W-model in Figure 1).

2.1. MPO Data

The MPO data set provides dense global coverage with ∼176.2 million vector measurements taken at an almost constant altitude decreasing from 422.1 km near the north pole to 348.6 km near the south pole, as measured above the mean planetary radius of 3393.5 km. Global coverage and data density were evaluated on a grid with bins of latitudinal size $\Delta\theta = 0.5°$ and longitudinal size

$$\Delta\phi = \frac{\Delta\theta}{\sin(\theta_c)} \tag{1}$$

where θ_c is the colatitude at the center of the respective bin, resulting in a grid with an average bin size of 870 km^2 at a radius of 3393.5 km. Data gaps remain only at the poles due to the MGS orbit inclination and the global coverage was found to be 99.8% with an average data density of 0.3899 km^{-2} when evaluated at a radius of 3393.5 km.

In order to decrease the influence of solar wind induced ionospheric currents, we rejected all MPO dayside data, leaving ∼56.3 million vector measurements at the nightside. The selection of nighttime data results in a polar data gap of 4.42° at the north pole and 2.86° at the south pole, with the asymmetry arising from different orbit altitudes at the poles.

In order to reduce the required computational cost, we selected one data point every 80 km along the surface footprint of the satellite track and a random offset at the beginning of each track was introduced to avoid a nonuniform data distribution. This selection resulted in ∼2.58 million data points on the nightside with unaltered global coverage and an average data density of 0.0179 km^{-2} projected on a sphere with a radius of 3393.5 km.

A priori data weights were estimated by making use of the stable MPO orbit, which allows for binning the data at a constant altitude and for subsequently calculating the variances in each bin. Bins of approximately the same surface area have been constructed using a quadrilateral grid (cf. equation (1)), and their size

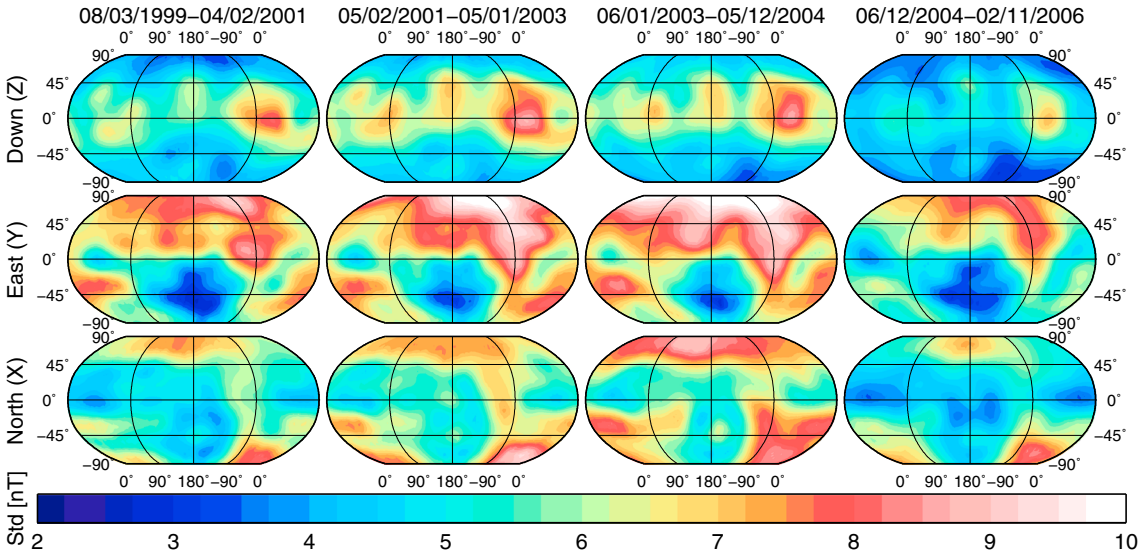

Figure 2. This figure shows the estimated standard deviations used as data weights for the MPO data at different epochs (columns) and for all magnetic field vector components (rows). Data weights are obtained by calculating the standard deviation of the data for each bin on a spatial grid with 0.5° resolution in latitude (cf. equation (1)), and subsequently fitting spherical harmonic functions up to degree and order 8 to obtain a smoothed representation of the standard deviations, which can be considered to be a measure for temporally variable nonlithospheric field contributions to the data.

has been chosen to be smaller than typical spatial variations of the lithospheric magnetic field at orbit altitude, but still containing as many data points as possible in order to obtain robust standard deviations. To achieve this, the largest acceptable bin size was found to be $\Delta\theta = 0.5°$, corresponding to surface areas of 867–883 km^2. Further, the data were divided into four epochs, each representing one Martian year with full global nightside coverage, as data variances are likely associated with solar wind-induced fields and related to solar activity. This division leads to an average number of 77–91 data points per bin for each of the four nighttime data sets.

The resulting standard deviations show a general global trend but vary considerably between neighboring bins. As the statistics of the errors are expected to vary continuously in space, we will assume that these strong bin-to-bin variations are due to an insufficient number of data points per bin. Therefore, the obtained values were weighted with the number of data points in each bin and fit to a set of global spherical harmonic functions up to degree and order 8. The resulting smoothed standard deviations for the horizontally north, east, and vertically down components for each of the four epochs are shown in Figure 2, and these are used to weight the MPO data in the inversion ($\mathbf{W}_d$ in equations (6), (7), (9), (10), and (14)).

Generally, the horizontal field components show larger standard deviations than the vertical field component and the latter has been identified to be less affected by external fields [*Luhmann and Brace*, 1991; *Acuña et al.*, 1999; *Arkani-Hamed*, 2004a]. Also, an anticorrelation with crustal field strength is observed for the horizontal field components, with lower standard deviations occurring above regions of stronger crustal fields. This may be related to the observation that current sheet crossings, which disturb the lithospheric field measurements, occur down to the MGS mapping orbit altitude mainly at regions of low field intensity [*Halekas et al.*, 2006]. Furthermore, differences between the four epochs are visible, suggesting a correlation with solar activity. From the first to the third epoch, the calculated standard deviations increase continuously, with a strong decrease for the fourth epoch. The first two epochs were within the maximum of solar cycle 23, while solar activity was continuously decreasing during the third and fourth epoch. However, geomagnetic storms were observed to be more frequent near the beginning of the declining phase of the solar cycle [*Echer et al.*, 2008, 2013], which could explain the large standard deviations of the third epoch under the assumption that geomagnetic storms are an indicator for magnetic activity at Mars.

2.2. AB/SPO Data

The aerobraking and science phase orbit data sets were obtained at strongly varying altitudes, providing only sparse coverage below MPO orbit altitudes. The low-altitude AB data were mainly obtained on the dayside, increasing the influence of solar wind-ionosphere interactions and therefore noise in the data [*Cain*

et al., 2003]. On the other hand, this data set provides a better resolution than the MPO data set, as the small scale contributions to the lithospheric field are significantly attenuated with increasing altitude.

During the AB/SPO mission phases, ~3.04 million vector measurements have been recorded, ~0.49 million of which were obtained at altitudes below the minimum MPO orbit altitude of 348 km. Of these, only 6.01% were taken during nighttime, mainly in the southern hemisphere at colatitudes greater than 120°. To reduce the contamination of the selected data by nonlithospheric field contributions, which dominate the crustal field down to an altitude of ~200 km at the dayside [*Brain et al.*, 2003], we rejected dayside data above this altitude. Overall, the selected AB/SPO data set contains ~0.29 million data points, consisting of the nightside data below 348 km and the dayside data below 200 km altitude. This data set provides a global coverage of 39.1% and an average data density of 0.0051 km^{-2} projected on a sphere with a radius of 3393.5 km.

Inspection of the residuals of the AB/SPO data to a preliminary model as well as to the model of *Langlais et al.* [2010] showed that three subsequent periapsis passes, occurring on 2 January 1999, between 02 h, 11 min and 09 h, 25 min UT, appear to have time stamp errors (cf. Figure S1 in the supporting information), and the respective data points have been removed from the final data set. However, no indication was found that this misalignment is a more general problem of the data set, although such a misalignment is hard to detect in regions of low field intensity.

The data variances of the AB/SPO data cannot be determined in the same way as for the MPO data, because the AB/SPO orbit altitude is not stable. Therefore, the respective variances were calculated from the residuals of the data to a preliminary model, which was based on the entire data set, derived without regularization, and using $\mathbf{W}_d = \mathbb{1}$ for the AB/SPO data (cf. equation (7) and W-model in Figure 1). By fitting a Gaussian distribution to the residuals and ignoring the outliers, standard deviations of 8.49 nT, 7.68 nT, and 6.97 nT were obtained for the horizontally north, east, and vertically down components of the dayside data, and 5.73 nT, 5.87 nT, and 5.25 nT for the same components of the nightside data (cf. Figures S2 and S3 in the supporting information). These values are lower than the values obtained by *Cain et al.* [2003], which were 6.2–7.1 nT for the nightside and 6.4–13.5 nT for the dayside AB/SPO data. This is probably because *Cain et al.* [2003] fit the Gaussian envelope to the entire distribution instead of explicitly disregarding the non-Gaussian tails as was done here.

3. Model and Inversion

In this paper we represent the lithospheric magnetic field of Mars by the gradient of a spherical harmonic expansion of the magnetic scalar potential including internal and external field contributions. The model is fit to the data by minimizing the functional Φ_{Data}, representing the difference between predicted and measured fields in a least squares sense, while outliers are handled using an appropriate measure of misfit. Nonlithospheric field contributions present in the lithospheric field model will be amplified when the model is downward continued and can lead to unrealistic small-scale oscillations in the model, therefore increasing model complexity, i.e., the amount of field variability in the model. In order to avoid such leakage of noise into the model, it is regularized by additionally minimizing a measure of model complexity at the surface, represented by the functional Φ_{Reg}. Here we use an iteratively reweighted least squares algorithm [*Farquharson and Oldenburg*, 1998], which approximates an absolute measure (L1 norm) to minimize Φ_{Reg}. This approach has the advantage that strong local magnetic anomalies are less smoothed out as when using a conventional squared distance measure (L2 norm).

The data are inverted by minimizing the functional Φ given by

$$\Phi = \Phi_{\text{Data}} + \Lambda_1 \Phi_{\text{Reg}} \tag{2}$$

with respect to the model parameters. Φ consists of the weighted sum of the contributions from the data Φ_{Data} and regularization Φ_{Reg}, and the damping parameter Λ_1 should be chosen such that the fit to the data and the term measuring the model complexity are well balanced.

The process of deriving the lithospheric field model is schematically shown in Figure 1, and we thoroughly describe the model and the technical details of the inversion such as the applied regularization technique in the following section.

3.1. Spherical Harmonic Model

Assuming no magnetic sources to be present at orbit altitude, the observed magnetic field $\mathbf{B}$ at satellite altitude can be expressed in terms of the gradient of a scalar potential field V with

$$\mathbf{B} = -\nabla V \tag{3}$$

The scalar potential V is separated in an internal part V_{int} and an external part V_{ext} with respect to the satellite's altitude and each part is expressed as a linear combination of spherical harmonic functions, truncated at a given degree and order L_{int} and L_{ext}, respectively, such that

$$\begin{aligned} V(r,\theta,\phi,t) &= V_{\text{int}}(r,\theta,\phi) + V_{\text{ext}}(r,\theta,\phi,t) \\ &= a\sum_{l=1}^{L_{\text{int}}}\left(\frac{a}{r}\right)^{(l+1)}\sum_{m=-l}^{l} g^m_{l,\text{int}} Y^m_l(\theta,\phi) \\ &\quad + a\begin{cases} \sum_{l=1}^{L_{\text{ext},n}}\left(\frac{r}{a}\right)^{l}\sum_{m=-l}^{l} g^m_{l,\text{ext},n} Y^m_l(\theta,\phi), & t \in t_{\text{night}} \\ \sum_{l=1}^{L_{\text{ext},d}}\left(\frac{r}{a}\right)^{l}\sum_{m=-l}^{l} g^m_{l,\text{ext},d} Y^m_l(\theta,\phi), & t \in t_{\text{day}} \end{cases} \end{aligned} \tag{4}$$

where $a = 3393.5$ km is the reference radius of the model and l and m are degree and order of the respective spherical harmonic function. A different external potential is used depending on local time (day or night), and L_{int} and $L_{\text{ext},d/n}$ are the maximum degree for the internal and external day/night expansion, and $g^m_{l,\text{int}}$ and $g^m_{l,\text{ext},d/n}$ are the internal and external day/night Gauss coefficients, respectively. We assume that these coefficients are constant, implying that no time-varying intrinsic field is present on Mars and seasonal variations of the external fields are ignored. Further, Y^m_l denote the Schmidt seminormalized spherical harmonic functions, where negative orders ($m < 0$) are associated with $\sin(m\phi)$ terms and zero or positive orders ($m \geq 0$) are associated with $\cos(m\phi)$ terms. The used spherical coordinate system is identical to the International Astronomical Unions standard for Mars and (r, θ, ϕ) are the radial distance, colatitude and longitude, respectively.

The external field represented by V_{ext} accounts for nonlithospheric field contributions, which exist in all data sets including the MPO nightside data [*Ferguson et al.*, 2005]. Indeed, a preliminary model ignoring external fields showed a significantly asymmetric distribution of the residuals, a clear indicator that the model did not account for all parts of the field. As the characteristics of the external fields are very different for the dayside and nightside [*Olsen et al.*, 2010], the use of two different external field models is necessary. However, it should be noted that the data are not sampling the entire magnetosphere due to the MGS-MPO Sun-synchronous orbit. Therefore, the external field model is rather absorbing noise than describing the physical characteristics of the external field. To avoid possible leakage of the lithospheric field into the external field model, a maximum degree and order of $L_{\text{ext},n} = 10$ was chosen for the nightside external field model. For the dayside model, which is based on the AB/SPO data set with lower data density and coverage, a maximum degree and order of $L_{\text{ext},d} = 5$ was chosen for the same reason.

The maximum degree L_{int} of the internal field model was chosen such that it represents well the sharp variations in the AB/SPO data set. As pointed out by *Cain et al.* [2003], a spherical harmonic (SH) expansion up to degree 90 is not sufficient, but with the limited amount of data available at that time, higher-degree models would have resulted in erroneous fields in sparse areas, which can now be avoided due to the very dense coverage of the MPO data set. In order to determine the maximum SH (Spherical Harmonics) degree L_{int} needed to accurately represent the data, we constructed models with L_{int} ranging from 90 to 130 in increments of 10. All models were derived from equally weighted AB/SPO data without regularization and an external field up to degree and order 10, regardless of dayside or nightside data (cf. equation (7) with $\mathbf{W}_d = \mathbb{1}$ and ABSPO$_{L\text{int}}$ models in Figure 1). For these models, we have calculated the resulting standard deviations of the residuals between model and data and found that the standard deviation decreases more slowly for degrees and orders larger than $L_{\text{int}} = 110$. In addition, we have investigated the residuals to these models on a track-by-track basis, and a selected aerobraking track is shown in Figure 3 as an example. Indeed, the model with a maximum SH degree of $L = 90$ shows significant deviations from the AB/SPO data, while the higher degree models perform much better. However, for some cases, such as for the east component at around 15 h, 20 m, 41 s, the higher the maximum SH degree, the better the data are fit.

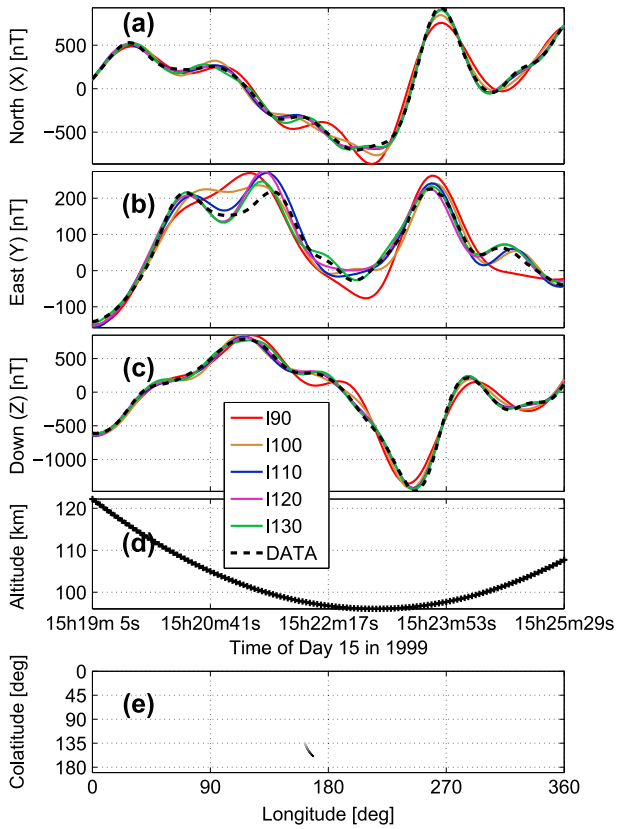

Figure 3. (a)-(c) Comparison of data and model fit along an aerobraking track for models with different maximum SH degree L_{int} and an external field up to degree $L_{ext} = 10$. The models were fitted solely to the AB/SPO data with equal weighting and without regularization. (d) Altitude and (e) location of the track. The $L = 90$ model shows large residuals to the data, while higher degree models perform significantly better. Some features, like the maximum in the east component at around 15h20m41s are fit the better the higher the maximum degree of the model.

Here we choose a maximum degree and order of $L_{int} = 110$, which we consider a good compromise between the ability to fit the sharp magnetic anomalies in the AB/SPO data and the necessary computational cost. We note, however, that a higher degree model will provide a better representation of some of the strong anomalies visible in the AB/SPO data and reveal more details in some areas.

3.2. Data Inversion

The problem of inverting vector magnetic field data consists of finding a set of Gauss coefficients g_l^m (cf. equation (4)), such that the given data will be fit by the model within its error limits. The corresponding forward problem, for which the model parameters $\mathbf{g}$, i.e., the Gauss coefficients, are known, is linear and can be written in matrix form as

$$\mathbf{Dg} = \mathbf{d} \tag{5}$$

where $\mathbf{d} = \left(d_1, d_2, ..., d_n\right)^T$ is the data vector, consisting of the $n = 2.87$ million data points, $\mathbf{g}$ is the model vector corresponding to the $m = L_{\text{int}}(L_{\text{int}} + 2) + L_{\text{ext},d}(L_{\text{ext},d} + 2) + L_{\text{ext},n}(L_{\text{ext},n} + 2) = 12475$ Gauss coefficients and $\mathbf{D}$ is a $n \times m$ matrix describing the spherical harmonic model as defined by equations (3) and (4).

The inverse problem corresponding to equation (5) cannot be solved directly, as the data contain noise and nonlithospheric field contributions. Therefore, we seek the weighted least squares solution using the data weighting matrix $\mathbf{W}_d$ by minimizing

$$\Phi_{\text{Data}} = (\mathbf{d} - \mathbf{Dg})^T \mathbf{W}_d^T \mathbf{W}_d (\mathbf{d} - \mathbf{Dg}) \tag{6}$$

with respect to $\mathbf{g}$. This results in the normal equations [*Aster et al.*, 2012]

$$\mathbf{g} = \left(\mathbf{D}^T \mathbf{W}_d^T \mathbf{W}_d \mathbf{D}\right)^{-1} \mathbf{D}^T \mathbf{W}_d^T \mathbf{W}_d \mathbf{d} \tag{7}$$

In order to obtain an unbiased solution to equation (7) under the assumption of normally distributed errors, the weighting matrix is chosen such that $\mathbf{W}_d^T \mathbf{W}_d = \mathbf{C}_d^{-1}$, where $\mathbf{C}_d$ is the covariance matrix of the data [*Aster et al.*, 2012]. Here we assume that errors are uncorrelated and that therefore $\mathbf{C}_d$ is diagonal and contains the variances of the errors of each data point. This may be an oversimplification, and one should in principle take the correlation between data errors into account. However, this would result in a nondiagonal covariance matrix $\mathbf{C}_d$ that cannot be handled easily even with modern computers.

Schmitz and Cain [1983] investigated the influence of inhomogenuous data sampling on the resulting correlations between model parameters and showed that these correlations can be minimized by considering the data density ρ in the weighting matrix. Correlations between model parameters are minimized for $(\mathbf{C}_d)_{ii} = \sigma_i^2 \rho_i$, where $(\mathbf{C}_d)_{ii}$ is the ith diagonal element of the data covariance matrix $\mathbf{C}_d$, while σ_i and ρ_i are the standard deviation and data density of the ith data point, respectively. Here the data density is evaluated on a grid with $\Delta\theta = 0.5°$ and $\Delta\phi = \Delta\theta / \sin\left(\theta_c\right)$, where θ_c is the colatitude at the center of the respective bin (cf. equation (1)).

3.3. Measure of Data Misfit

Data outliers can have a negative influence on the resulting model, which can be avoided by removing outliers a priori. However, it is difficult to decide which data points can be regarded as such. Alternatively, one may relax the assumption that errors are normally distributed. Here we use a threshold misfit value δ_c to distinguish between the normally distributed part of the data and data outliers. The corresponding unnormalized probability density function is given by

$$L(x) = \begin{cases} \exp\left(-x^2\right) & , |x| \leq \delta_c \\ \exp\left(\frac{-2|x|^\alpha \delta_c^{(2-\alpha)}}{\alpha} + \frac{(2-\alpha)\delta_c^2}{\alpha}\right) & , |x| > \delta_c \end{cases} \tag{8}$$

where x is the data misfit and α determines the characteristics of the shape of the distribution such that lower values of α will have a larger tail. In particular, for $\alpha = 2$, $L(x)$ will be equal to a normal distribution, and for $\alpha = 1$, $L(x)$ will be equal to the distribution originally suggested by *Huber* [1964]. This probability density function leads to a measure of misfit which can be implemented using iteratively reweighted least squares. The objective function can then be written as [*Farquharson and Oldenburg*, 1998]

$$\Phi_{\text{Data}} = (\mathbf{d} - \mathbf{Dg})^T \mathbf{W}_d^T \mathbf{M}_d \mathbf{W}_d (\mathbf{d} - \mathbf{Dg}) \tag{9}$$

which leads to the following normal equations

$$\mathbf{g} = \left(\mathbf{D}^T \mathbf{W}_d^T \mathbf{M}_d \mathbf{W}_d \mathbf{D}\right)^{-1} \mathbf{D}^T \mathbf{W}_d^T \mathbf{M}_d \mathbf{W}_d \mathbf{d} \tag{10}$$

where the misfit matrix $\mathbf{M}_d$ is diagonal with

$$\left(\mathbf{M}_d\right)_{ii} = \begin{cases} 1 & , |x_i| \leq \delta_c \\ \left(\delta_c / |x_i|\right)^{2-\alpha} & , |x_i| > \delta_c \end{cases} \tag{11}$$

and $x_i = \left(\mathbf{W}_d \left(\mathbf{d} - \mathbf{Dg}\right)\right)_i$.

3.4. L1 Regularization

As part of the magnetic field $\mathbf{B}$ originates from internal sources and the strength of a component of degree l is hence proportional to $r^{-(l+2)}$ (equations (3) and (4)), short wavelength lithospheric field contributions are preferentially attenuated with increasing altitude r and the resulting lithospheric part $\mathbf{B}_{\text{int}}$ of the magnetic field $\mathbf{B}$ will appear smoother further away from the sources. Therefore, the intensity of lithospheric small-scale fields can fall below the noise level in the data at orbit altitude and the model will fit a significant part of the noise for high harmonic degrees. Consequently, when the model is downward continued to the planetary surface, unrealistically intense global magnetic features of short wavelengths will appear, which are usually oriented along the satellite orbit tracks [*Lesur et al.*, 2013]. Here we regularized our model to limit this effect.

Though it has been argued that models expanded to high harmonic degrees do not improve the achievable resolution due to noise in the data and should therefore be truncated accordingly [*Arkani-Hamed*, 2002b, 2004a], information present in higher degrees can be extracted at least locally if the model is properly regularized. One possibility to do so is to additionally minimize some measure of the resulting model complexity [*Parker*, 1994; *Aster et al.*, 2012], which is a priori information on the model. Here we chose to minimize the roughness of the surface field and use an approximation of the surface integral of the absolute horizontal gradient ∇_H of the vertically down lithospheric field component Z_{int} (cf. equation (13)) as a measure for model complexity. Such an integral defines a norm and can therefore be used, as any other norm, to reduce model complexity [*Shure et al.*, 1982].

We use an iteratively reweighted least squares (IRLS) algorithm in order to approximate an L1 norm minimization of model complexity [*Farquharson and Oldenburg*, 1998]. With the chosen measure of model complexity, the use of an L1 norm for regularizing the model implies that the horizontal gradient of the vertically down lithospheric field component Z_{int} is assumed to follow a Laplacian distribution over the Martian surface. This assumption is based on the observation that localized anomalies with large field gradients are common on Mars. In other words, the L1 norm regularization places a weaker constraint on strong localized gradients when compared to a quadratic measure. This allows for sharp lithospheric field gradients to be

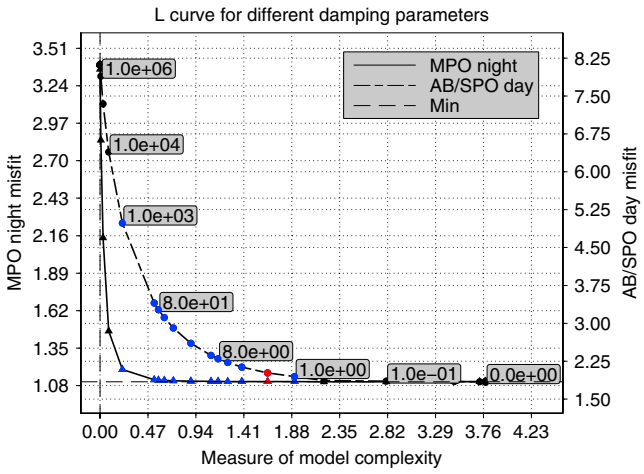

Figure 4. Weighted data misfit for MPO data (left ordinate and solid line) and AB/SPO data (right ordinate and dashed line) versus the chosen measure of model complexity (normalized by $4\pi R_p^2$) for different damping parameters Λ_1. For each obtained value of model complexity the damping parameter is depicted by a circle and a triangle, corresponding to the AB/SPO dayside and the MPO nightside misfit, respectively. For some models, the damping parameter is also indicated numerically. Large damping parameters tend to significantly increase the misfit to the data, while small damping parameters lead to models with large model complexity, without significantly improving the data misfit. Therefore, the damping parameter should be chosen near the bend of the L-shaped curve, and the admissible damping parameters are shown in blue. Among these, the selected damping parameter $\Lambda_1 = 2$ is shown in red.

maintained, if the regularization is applied in physical space. As it is not possible to use an analytic solution for regularization when an IRLS algorithm is used, we evaluated the horizontal lithospheric field gradient of Z_{int} numerically. We calculated $Z_{\text{int}} = \partial V_{\text{int}}/\partial r$ on a hexagonal grid, which results in an homogeneous sampling of the lithospheric field on the mean planetary radius (3393.5 km) in the spatial domain. The resolution of the grid has been chosen such that there are at least twice as many grid points than model parameters, and 81,920 grid points have been used. The horizontal gradient is then calculated using finite differences in the $\mathbf{e}_\phi$ and $\mathbf{e}_\theta$ direction using equations (3) and (4). Formally, the entire operation of calculating $\nabla_H Z_{\text{int}}$ can then be described by the linear operator $\mathbf{R}$, such that

$$\left[\nabla_H Z_{\text{int}}\right]_{\{i\}} = \mathbf{R}\mathbf{g} \tag{12}$$

where $\left[\nabla_H Z_{\text{int}}\right]_{\{i\}}$ is the set of horizontal gradients evaluated at each of the grid points i, and $\mathbf{R}$ operates on the internal field coefficients $\mathbf{g}_{\text{int}} \subset \mathbf{g}$.

The objective function for the regularization including IRLS to approach an absolute measure (L_1) of model complexity is finally given by

$$\Phi_{\text{Reg}} = \mathbf{g}^T\mathbf{R}^T\mathbf{W}_r^T\mathbf{M}_r\mathbf{W}_r\mathbf{R}\mathbf{g} \approx \int_\Omega \left|\nabla_H Z_{\text{int}}(r=a,\theta,\phi)\right| dS \tag{13}$$

where the diagonal weighting matrix $(\mathbf{W}_r)_{ii} = \sqrt{s_i}$ has been introduced to account for the surface areas s_i corresponding to each of the grid points i and the diagonal misfit matrix $\mathbf{M}_r$ is given by $\left(\mathbf{M}_r\right)_{ii} = 1/|x_i|$ with $\mathbf{x}_i = \left(\mathbf{W}_r\mathbf{R}\mathbf{g}\right)_i$ [*Farquharson and Oldenburg*, 1998].

3.5. Summary

Overall, the lithospheric magnetic field model is obtained by minimizing equation (2), using equations (9) and (13), leading to the normal equations

$$\mathbf{g} = \left(\mathbf{D}^T\mathbf{W}_d^T\mathbf{M}_d\mathbf{W}_d\mathbf{D} + \Lambda_1\mathbf{R}^T\mathbf{W}_r^T\mathbf{M}_r\mathbf{W}_r\mathbf{R}\right)^{-1} \mathbf{D}^T\mathbf{W}_d^T\mathbf{M}_d\mathbf{W}_d\mathbf{d} \tag{14}$$

which were solved for the Gauss coefficients $\mathbf{g}$ using QU factorization.

Using iteratively reweighted least squares both in the data and regularization term requires iterating the solution, which is computationally expensive. Therefore, we used a series of simpler models to derive the following model parameters: the maximum SH degree and order L_{int} for the internal model, the data weights for the AB/SPO data set, and the damping parameter Λ_1 (cf. Figure 1).

The damping parameter Λ_1 controls the trade off between model smoothness and fit to the data. It was obtained from a parameter study based on a model with $\mathbf{M}_d = \mathbb{M}_d = \mathbb{1}$ (i.e., L2 model in Figure 1 with L2 regularization). In Figure 4, the adopted measure of model complexity (left side of equation (13) with $\mathbb{M}_d = \mathbb{1}$), normalized by $4\pi R_p^2$, is plotted against the MPO (solid line with triangles) and AB/SPO daytime (dashed line with circles) weighted data misfit for different damping parameters Λ_1, as indicated in the

Table 1. Values of the Parameters δ_c and α of Equation (8) for the Measure of Data Misfit and the Treatment of Data Outliers[a]

Data Set	Component	δ_c	α
MPO	*X*	2.0	0.1
night	*Y*	2.0	0.1
($\Delta_d = 80$ km)	*Z*	2.2	0.1
AB/SPO	*X*	1.0	2.0
day	*Y*	1.0	2.0
(h $\leq$ 200 km)	*Z*	1.0	2.0
AB/SPO	*X*	1.0	2.0
night	*Y*	1.0	2.0
(h $\leq$ 348 km)	*Z*	1.0	2.0

[a]The respective values were determined from a fit to the residual histogram of a preliminary model with $\delta_c = 0$ and $\alpha = 2$ (L1 model in Figure 1). In the column labeled "Data Set", *h* is altitude and Δ_d is the distance between subsequent data points as measured on the satellite's projected surface track. *X*, *Y*, and *Z* refer to the horizontally north, east, and vertically down components of the magnetic field, respectively.

gray boxes. Depending on Λ_1, two regimes can be distinguished: For $\Lambda_1 > 1000$, the measure of model complexity remains almost constant, while the misfit to the data significantly increases with increasing Λ_1. On the other hand, for $\Lambda_1 < 1$, the data misfit remains almost constant while regularization misfit and therefore model complexity increase with decreasing Λ_1. In this regime, anomalies that are poorly defined by the data will be suppressed in the resulting model without significantly decreasing the fit to the data. For the MPO data (solid line), the data misfit remains almost constant even for stronger damping up to $\Lambda_1 = 100$. This was already observed by *Whaler and Purucker* [2005] and may reflect that the higher-altitude data are less sensitive to small-scale fields at the surface and contains less noise than the AB/SPO dayside data. As we seek a model which reasonably fits the data without overfitting noise, a damping parameter in the range $1 \leq \Lambda_1 \leq 1000$ (shown in blue in Figure 4) is considered a good compromise between data misfit and model smoothness. As we apply an iteratively reweighted least squares algorithm to approach an absolute measure of model complexity (cf. equation (13)), which will suppress noise more efficiently than the least squares measure used in Figure 4, a damping parameter at the lower end of the acceptable range is appropriate. Therefore, we choose a damping parameter of $\Lambda_1 = 2$. The exact value of the chosen damping parameter sensitively influences the details of the resulting model. For example, a damping parameter at the upper end of the acceptable range would result in a significantly stronger regularized model, with much less detail in the regions of high field intensity, but very little noise.

Subsequently, we applied the L1 regularization using the chosen damping parameter and adapted it to the new weights in $\mathbf{M}_r$, such that a model with $\mathbf{W}_d = \mathbb{1}$ was obtained after 10 iterations (L1 model in Figure 1). Finally, the shape of $\mathbf{M}_d$ was determined by varying the parameters δ_c and α such that the associated error distribution (cf. equation (8)) is a suitable representation of the resulting distribution of the residuals between the data and the L1 model. The results for δ_c and α for each data set and component of the magnetic field can be found in Table 1 and the respective histograms for the MPO data set can be found in Figure S4 in the supporting information. For the AB/SPO data, the chosen values correspond to an L2 norm (i.e., $\mathbf{W}_d = \mathbb{1}$), although the corresponding residuals show large non-Gaussian tails. However, a significant part of the large residuals in the AB/SPO data is due to an insufficient maximum spherical harmonic degree and order. Applying the modified Huber weights would therefore further decrease the fit for some of the sharp variations in the AB/SPO data, which would then be treated as data outliers. As an example, the process of choosing δ_c and α is shown in Figure 5 for the vertically down component of the MPO nighttime data. The histogram of the weighted data is shown in blue, the associated Gaussian distribution in red, the cut off value δ_c by the squares on the ordinate and the distribution for the treatment of data outliers is shown in black. The linear plot on the right-hand side focuses on the normally distributed part of the data (red line), whereas the logarithmic plot on the left-hand side focuses on the tails of the distribution (black line). It is clearly visible that the resulting distribution of the residuals deviates significantly from a Gaussian distribution for large misfit values and that the applied probability density function (PDF) is supported by the data. With the values for δ_c and α obtained in this way, two further iterations were made in order to obtain the favored model (green box in Figure 1).

4. Results

We constructed a model of the lithospheric magnetic field of Mars based on an expansion of the magnetic scalar potential into spherical harmonic functions up to degree and order 110. Models for the static external fields for the dayside and nightside were derived up to maximum degree and order 5 and 10, respectively. The model is based on nighttime data of the entire MGS mapping phase orbit period and data from the

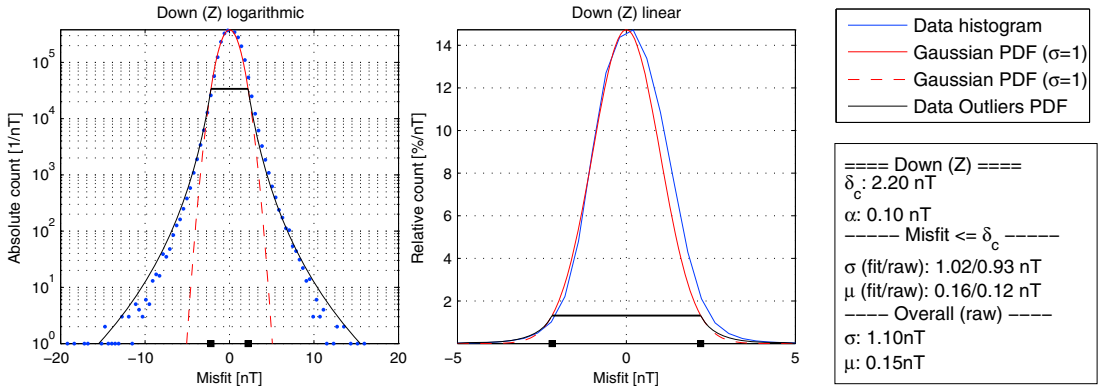

Figure 5. Histogram of the weighted residuals for the vertically down component of the MPO nighttime data to a model with $\mathbf{W}_d = \mathbb{1}$ and $\Lambda_1 = 2$ (L1 model in Figure 1), outlined with (left) blue dots and (right) a blue line. Figure 5 (left) shows a logarithmic representation, while Figure 5 (right) shows a linear plot. For a misfit smaller or equal to δ_c, a normal distribution with standard deviation $\sigma = 1$ nT and mean $\mu = 0$ nT is assumed (red line). The black line corresponds to the probability density function (PDF) of equation (8) for a misfit larger than δ_c. The threshold value δ_c is indicated by the black squares on the ordinate. In the box on the right-hand side, δ_c and α (cf. equation (8)) as well as the standard deviation σ and mean μ of all residuals (Overall) and the residuals with a misfit smaller than δ_c (Misfit $\leq \delta_c$) are given. In the latter case, σ and μ have been calculated from a Gaussian fit to the distribution (labelled fit) and the misfit values themselves (labelled raw). As is evident from the figure, the residuals are not well represented by a normal distribution for large values of misfit, but the adapted PDF of equation (8) is a suitable representation.

AB/SPO mission phases below 200 and 384 km altitude on the dayside and nightside, respectively. Data outliers were treated by applying a modified Huber-Norm, and the model was regularized by using an IRLS algorithm, which approximates the minimization of the absolute measure (L1 norm) of the horizontal gradient of the vertically down field component at the surface. This has the advantage that strong magnetic anomalies such as present on Mars will be less suppressed compared to using a conventional L2 measure for regularization.

In the following section, we will present the model at surface altitude and discuss the statistics of the residuals between the data and the model as well as the resulting model power spectrum. Furthermore, we will present some isolated magnetic field anomalies, the magnetic field over a region of previously unrecognized volcanic calderas, and some examples of impact-demagnetized crust. These examples are intended to show how this model can help to improve our knowledge of the past and present Martian magnetic field.

4.1. Surface Field

In Figure 6, the resulting model of the lithospheric magnetic field is shown for all three vector components at the model reference radius of $r = 3393.5$ km, corresponding to the mean planetary radius of Mars. In the map, the major impact basins (from left to right: Hellas, Isidis, Utopia, and Argyre) are indicated by black-dashed lines and the topographic dichotomy is represented by a solid contour line along the 0 m isoline as defined in the Mars Orbiter Laser Altimeter (MOLA) data.

The presented model reproduces the known features of the Martian lithospheric field. In particular, the magnetic field over the outlined major impact basins and major volcanic provinces of Tharsis and Elysium is negligible. Further, the northern lowlands exhibit lower magnetic field strengths than the southern highlands, where peak intensities of ~12000 nT are reached, corresponding to twice the lower bound value of ~6000 nT reported by *Langlais et al.* [2004]. Owing to the higher SH degree and regularization through approaching an L1 norm, the map shows a comparatively high level of detail while simultaneously suppressing small-scale noise.

4.2. Statistics

A straightforward measure of the quality of the fit to the data is given by the residuals, i.e., the difference between model predictions and the respective observations. If the a priori data errors σ_i are considered, the weighted residuals are given by

$$r_i = \frac{\mathbf{d}_i - \sum_j \mathbf{D}_{i,j}\mathbf{m}_j}{\sigma_i} \tag{15}$$

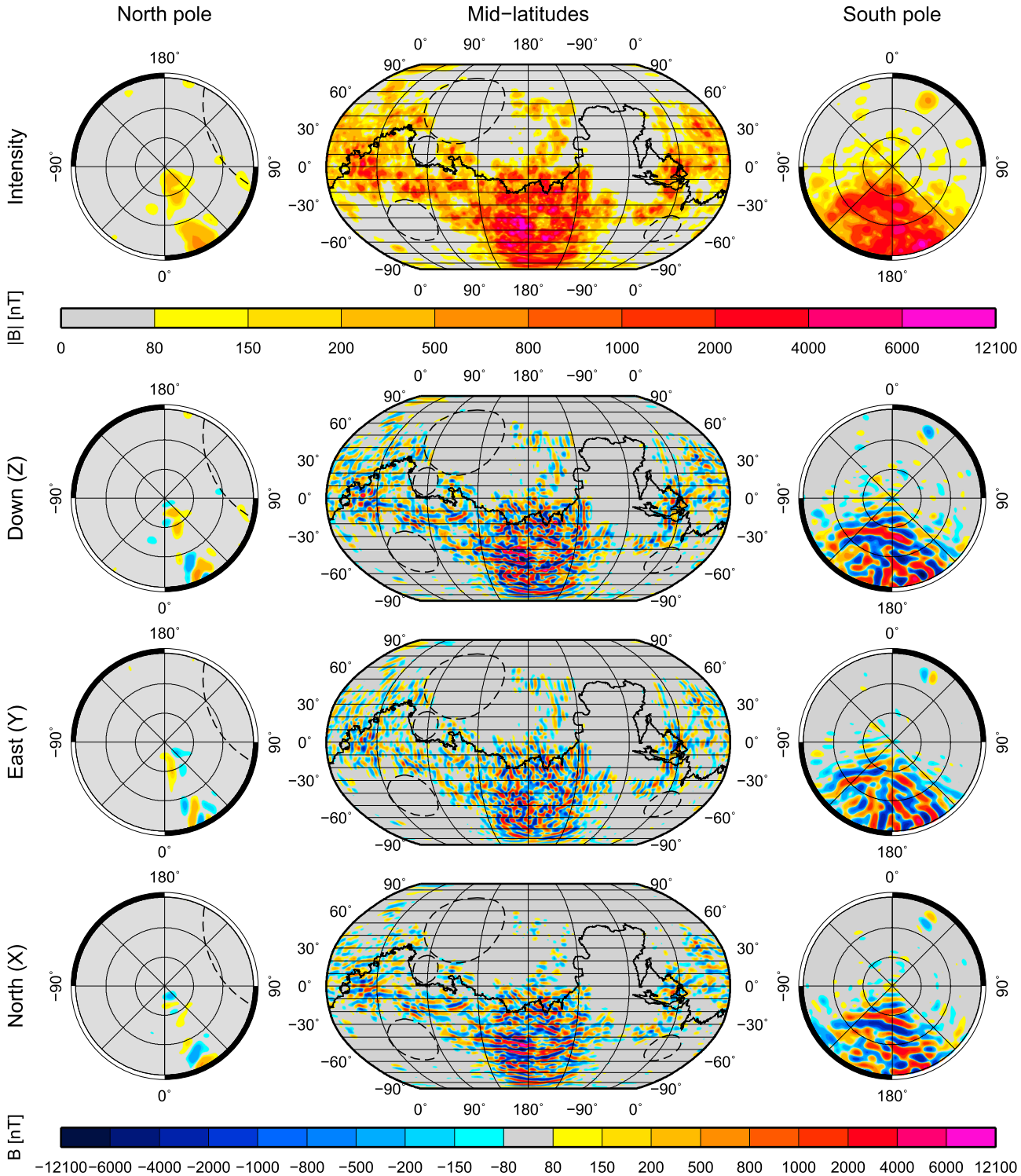

Figure 6. Map of the lithospheric part of the magnetic field model evaluated at the mean planetary radius of 3393.5 km. (top to bottom) The magnetic field intensity, and the vertically down (*Z*), horizontally east (*Y*), and north (*X*) components are shown. (left to right) The north pole, midlatitudes, and the south pole are presented. Major impact basins are indicated by dashed lines, while the thick black line represents the zero level of MOLA topography, indicating the topographic dichotomy boundary.

Table 2. Statistics of the Model fit (Favored Model in Figure 1) for Different Data Sets and the Horizontally North (*X*), East (*Y*), and Vertically Down (*Z*) Magnetic Field Components[a]

Data Class		This Study					*Langlais et al.* [2004]			*Cain et al.* [2003]		
		σ	σ^w	μ	μ^w	ρ	σ	μ	ρ	σ	μ	ρ
MPO	*X*	6.42	1.11	0.43	0.07	0.91	6.70	0.74	0.91	6.74	0.87	0.90
night	*Y*	7.20	1.12	−0.36	−0.07	0.83	7.31	0.28	0.83	7.37	−0.36	0.82
$\Delta_d = 80$ km	*Z*	5.90	1.09	0.81	0.15	0.95	6.33	0.42	0.94	6.28	0.86	0.94
AB/SPO	*X*	9.78	1.71	−1.65	−0.29	0.99	14.80	−0.82	0.97	17.98	−2.78	0.96
night	*Y*	8.62	1.47	−0.32	−0.05	0.98	15.03	0.03	0.94	17.42	0.35	0.93
(h ≤ 348 km)	*Z*	8.86	1.69	−0.69	−0.13	0.99	20.21	0.63	0.97	15.81	−0.14	0.98
AB/SPO	*X*	16.77	1.98	−2.28	−0.27	0.96	20.81	−3.75	0.94	12.45	−0.85	0.98
day	*Y*	16.92	2.20	0.24	0.03	0.94	20.87	0.20	0.90	10.52	−0.29	0.97
(h ≤ 200 km)	*Z*	14.03	2.01	−0.75	−0.11	0.98	22.22	−1.12	0.95	13.54	−0.24	0.98

[a]The standard deviation of the residuals is given by σ, the average value of the residuals is given by μ and the correlation coefficient between data and model predictions is given by ρ. The superscript *w* indicates that the respective values were weighted with their a priori data weights as described in section 2. For comparison, the unweighted values are also shown for other published models.

where *i* refers to the *i*th datum and *j* to the *j*th model parameter. This equation transforms to the case of unweighted residuals if $\sigma_i = 1 \; \forall \; i$. The standard deviation of the weighted residuals will approach one if the a priori data weights σ_i (cf. $\mathbf{W}_d$ in equations (6) and (14)) have been correctly chosen and the error distribution is indeed normal. Also, the mean value of the residuals should be zero for an unbiased solution. In addition, we compute the correlation coefficient between the model and the data [*Purucker et al.*, 2000; *Langlais et al.*, 2004], with perfect correlation resulting in a correlation coefficient of one. However, it should be noted that the correlation coefficient does not account for systematic offsets.

In Table 2, the mean values μ, standard deviations σ, and correlation coefficients ρ of the weighted and unweighted residuals are given for different data sets as obtained from the presented model. For comparison, the respective unweighted values are also given for the models of *Langlais et al.* [2004] and *Cain et al.* [2003]. However, as these studies used different data sets, numerical values should not be compared directly, but rather indicate differences in the way the models were derived.

For the presented model, the unweighted standard deviations of the vertically down component of the magnetic field *Z* are generally smaller than those of the horizontal components, except for the AB/SPO nighttime data, which is in agreement with previous studies. Also, the AB/SPO dayside data show larger unweighted standard deviations compared to the corresponding nightside data, reflecting the influence of solar wind-induced fields. Concerning the weighted residuals, the data-based determination of a priori weights for the MPO data is working well, as the respective standard deviations are close to unity. This is not the case for the AB/SPO data, where larger values may reflect a contribution of the significantly non-Gaussian tails in the residual distribution. Despite accounting for static external fields, the residual mean values deviate from zero. For the MPO data, the largest mean value of 0.81 nT is reached for the vertically down component, whereas for the AB/SPO data, the largest offset of −2.28 nT is observed for the horizontal north component. Any offset from zero hints at unmodelled fields in the data, e.g., ionospheric or magnetotail plasma currents, which result in nonstatic external field contributions.

Compared to the model of *Langlais et al.* [2004], the presented model generally achieves slightly lower standard deviations, especially for the AB/SPO data, while the mean value of the unweighted residuals is higher in some cases. The model of *Cain et al.* [2003], on the other hand, is offering the best fit to the AB/SPO dayside data in all considered aspects, while the fit to the MPO and AB/SPO nightside data is poorer when compared to the presented model and the horizontal components of the model of *Langlais et al.* [2004]. This may be due to the data selection procedure of *Cain et al.* [2003], who only used MPO nightside data to fill the gaps of the AB/SPO data set, leading to a nonglobal selection of MPO data. Although the AB/SPO data were taken at lower altitudes, they contain significant contributions from nonlithospheric fields, which can easily leak into the lithospheric field model. A better fit to the AB/SPO data therefore does not necessarily result in a better model, especially if the AB/SPO fit is achieved at the cost of a poor fit to the less noisy MPO data.

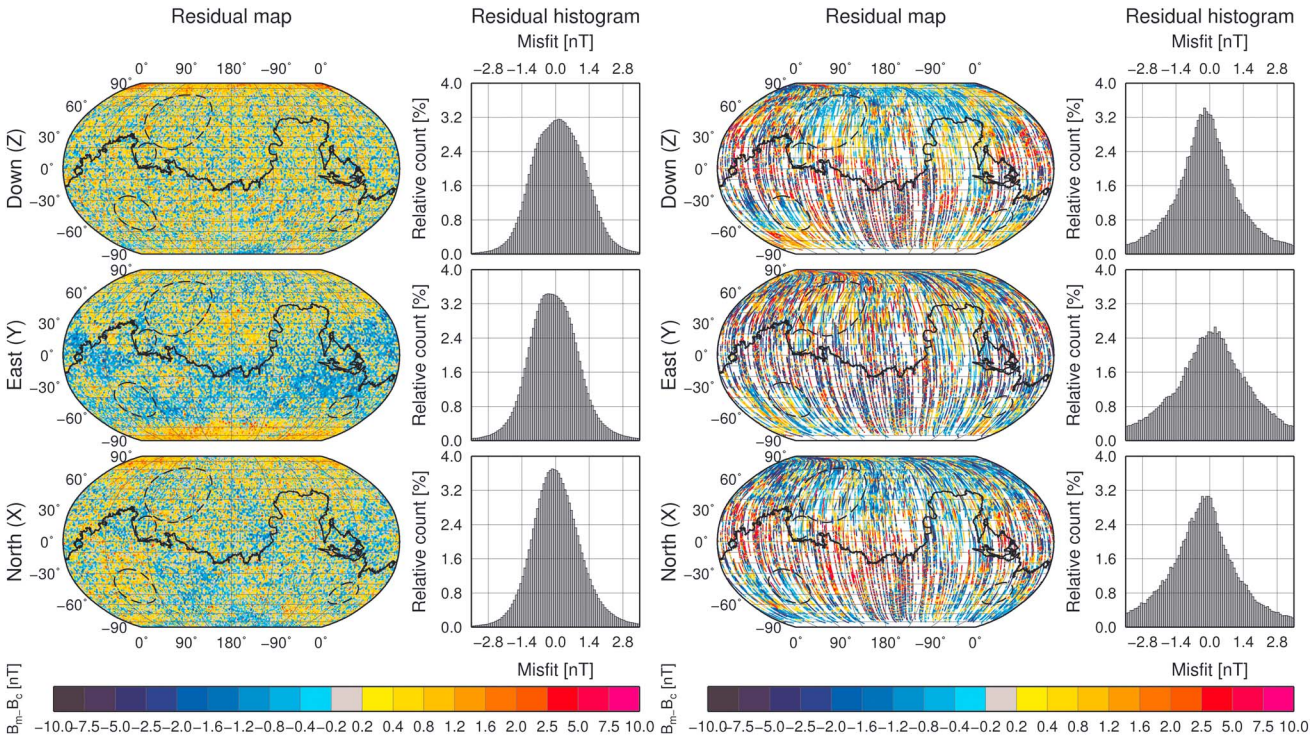

Figure 7. Weighted residuals of the final model for the (left) MPO nighttime and (right) AB/SPO daytime data sets for each of the three vector components of the Martian lithospheric magnetic field. Along with the spatial distribution, histograms of the residuals are shown. For the MPO data set, the spatial distribution is fairly homogeneous, especially for the least disturbed vertically down component. For the AB/SPO data set, on the other hand, small-scale patterns are present in the region of high field intensity over Terra Cimmeria and Terra Sirenum. This may indicate that a higher SH degree model would be justified to represent the data.

4.3. Spatial Distribution of the Residuals

A map of the spatial distribution of the weighted residuals (cf. equation (15)) along with the respective histograms for all three vector components of the MPO nighttime magnetic field data is shown in Figure 7 (left). For the vertically down component *Z*, the residuals are homogeneously distributed, indicating that most of the static external field contributions have been accounted for in the model. For the horizontal components, however, some large-scale spatial correlations are visible. These correlations may indicate that quasi-static external fields are slowly changing with solar activity and the static external field model is therefore not able to represent the external field at all times. Indeed, examining the residuals obtained separately for the epochs shown in Figure 2 revealed significant variations with respect to time, in particular for the horizontal components. Therefore, these large-scale correlations may reflect the fact that quasi-static external fields are mostly aligned with the horizontal field components and vary with solar activity.

For the AB/SPO data, a similar map is shown in Figure 7 (right). Here the resulting data histograms have significantly larger tails than it is the case for the MPO data. Also, spatial correlations in the residuals are visible for all three vector components, likely reflecting the increased influence of nonlithospheric fields. Over the largest fields at Terra Cimmeria and Terra Sirenum around the 180° meridian in the southern hemisphere, the residuals show patterns at the scale of the lithospheric field, which indicates that a potential field expansion up to a degree and order higher than 110 is necessary to fit adequately the AB/SPO data above the regions of highest field intensity.

4.4. Power Spectrum

The Mauersberger-Lowes power spectrum [*Mauersberger*, 1956; *Lowes*, 1966] is a spectral measure of the mean square field in the spherical harmonic domain and is shown in Figure 8 for different models, evaluated at the reference radius of 3393.5 km. The lithospheric field model derived here is shown in solid black with the nightside and dayside external fields in dashed and dotted black lines, respectively. For comparison, the power spectra of the L2 model, which was derived using the conventional least squares regularization

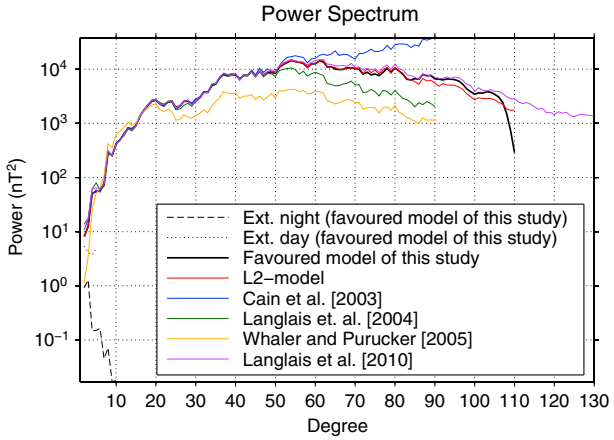

Figure 8. Mauersberger-Lowes power spectrum for different lithospheric field models evaluated at the mean Martian radius of 3393.5 km. The presented model is shown in black along with the external nighttime and daytime fields in dashed and dotted black lines, respectively. The corresponding model with least squares regularization (L2 model) is shown in red. For comparison, the models of *Cain et al.* [2003], *Langlais et al.* [2004], *Whaler and Purucker* [2005], and *Langlais et al.* [2010] are also shown.

(cf. Figure 1) as well as the SH model of *Cain et al.* [2003] are also shown. In addition, the power spectrum of the magnetization models of *Langlais et al.* [2004], *Whaler and Purucker* [2005], and *Langlais et al.* [2010] are shown, which have been derived using an equivalent spherical harmonic representation of their predicted lithospheric magnetic field.

The shapes of the different presented power spectra are very similar, and the respective peaks and troughs occur in most cases at the same SH degree. Up to degree 46, the power spectrum of the presented model (favored model in Figure 1) falls within 1000 nT^2 of the other published models shown in Figure 8, except for the model of *Whaler and Purucker* [2005], which has systematically less power for degrees $l > 16$ compared to all other models, with a maximum difference of ~8000 nT^2. Generally, for degrees above $l > 46$, the power spectra of the different models start to diverge due to noise becoming important compared to the lithospheric signal. Compared to the L2 model of our study, the favored one shows a strong drop-off of ~2800 nT^2 for degrees $l > 106$, which is a result of the L1 regularization.

The nightside external field model falls off very quickly with increasing SH degree. The dayside external field model, on the other hand, is stronger and contributes a significant amount of power to the overall dipolar and quadrupolar terms. The slight increase of power at $L_{ext,d} = 5$ may indicate that power of higher degrees is dissipating to lower degrees due to model truncation.

4.5. Performance of the L1 Norm

We regularized the model by using an IRLS algorithm in order to approach an absolute measure (L1 norm) of model complexity. This approach supports strong localized gradients of the magnetic field and the efficiency of the L1 norm can be tested by comparing the final model to a model with $\mathbf{M}_d = \mathbb{M}_d = \mathbb{1}$ (cf. L2 model in Figure 1), which uses L2 regularization.

In Figure 9, the vertically down magnetic field component is shown on the surface (a–d) and at 150 km altitude (e–h) for different models in a region with areas of strong and weak magnetic fields. This region includes the Apollinaris Patera volcano (cf. black frame in Figure 9e), which has previously been associated with a magnetic and gravity anomaly and which has been investigated in more detail by *Langlais and Purucker* [2007] and *Hood et al.* [2010]. In order to demonstrate the effectiveness of the L1 regularization, the model presented here (favored model in Figure 1) is compared to a model using L2 regularization and equivalent damping (L2 model in Figure 1). In the northern part of the map, which is dominated by low field strengths, anomalies elongated in the north-south direction are observed for the L2 model (Figure 9b). These elongated anomalies are approximately aligned with the satellite track and are typical for correlated noise leaking into the model [*Lesur et al.*, 2013]. The model presented here (Figures 9a and 9e) effectively suppresses this noise, whereas the strong lithospheric anomalies in the southern part of the map keep their structure and peak strengths. This is confirmed by Figure 9i, where the vertically down magnetic field component at surface altitude is shown along the parallel of 18°*S* (cf. dashed line in Figure 9a) for the favored model of this study with L1 regularization (red line) and the L2 model with L2 regularization (black line). This comparison shows that the applied regularization technique is indeed able to maintain strong anomalies while effectively damping noise in the model.

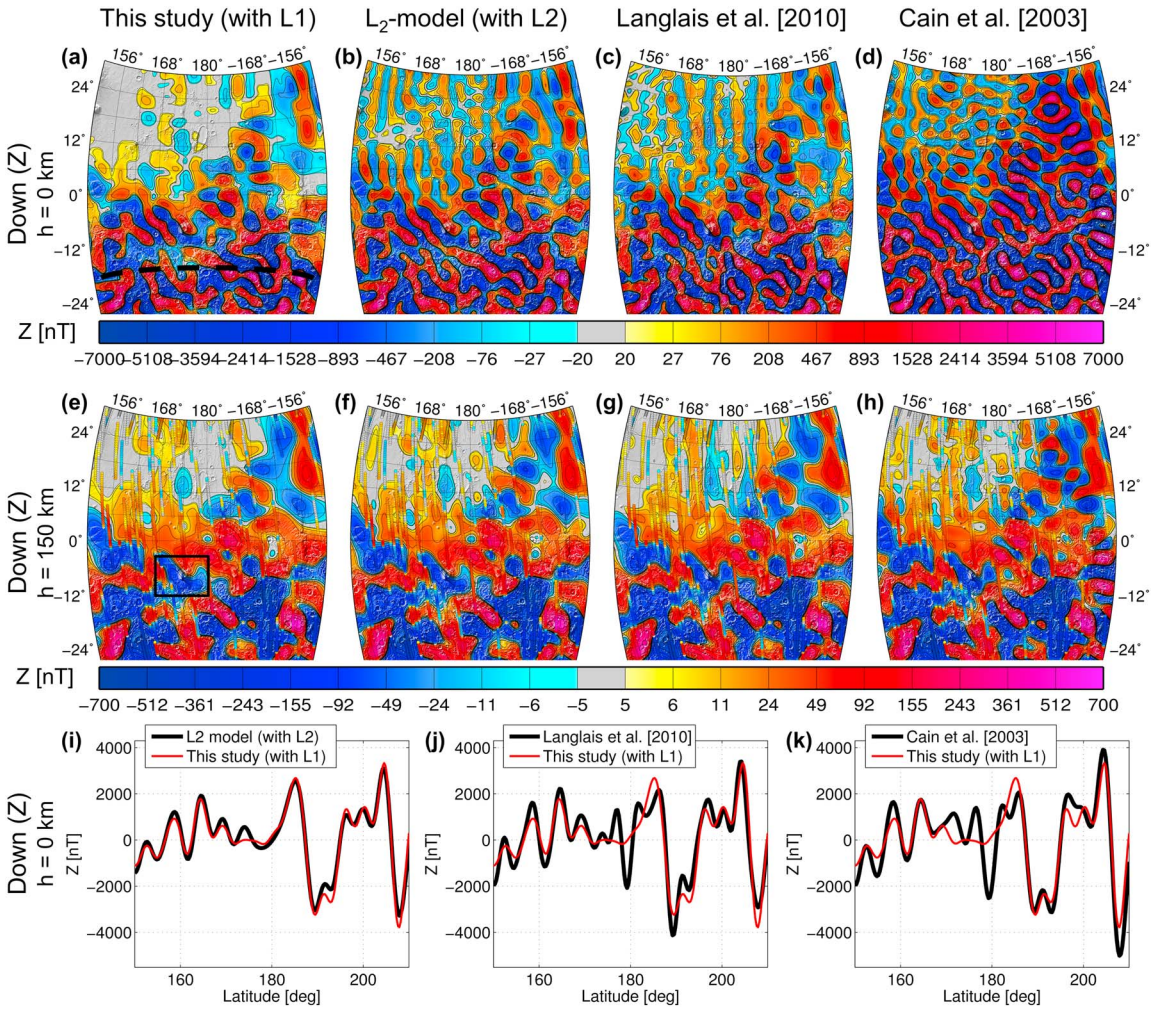

Figure 9. Map of the lithospheric vertically down magnetic field component for different models and altitudes of (e–h) 150 km and (a–d) 0 km above the surface altitude. The map is centered at 180°*E* and 0°*S*, close to the ancient volcano Apollinaris Patera, and plotted over shaded MOLA topography. In the higher altitude maps, shown in Figures 9e–9h, the AB/SPO data with altitudes of 150 ± 30 km is overlaid and plotted along track with circles. The Apollinaris Patera volcano is located southwest of the map's center and indicated by the black rectangle in Figure 9e. (i–k) The vertically down magnetic field component is shown at surface altitude for different models along a parallel of 18°*S*, as indicated by the dashed line in Figure 9a.

For comparison, the respective maps derived from the models of *Langlais et al.* [2010] and *Cain et al.* [2003] are shown in Figures 9c and 9g and Figures 9d and 9h and the vertically down magnetic field component along the parallel of 18° *S* is shown by the black lines in Figures 9j and 9k, respectively. As the model of *Langlais et al.* [2010] is based on equivalent source dipoles, it cannot be downward continued to the surface, and a spherical harmonic representation up to degree and order 130 of the dipole model has been used instead to produce the presented map at surface altitude. At both altitudes, the model by *Langlais et al.* [2010] looks very similar to the L2 model of this study. The model of *Cain et al.* [2003], on the other hand, produces similar results as the other models at 150 km altitude, but significantly more noise is visible at surface altitude, which is partly due to AB/SPO data gaps.

4.6. Isolated Magnetic Anomalies

Isolated crustal anomalies have been used to study magnetic pole reversals and paleopole positions, which can provide information on the dynamics of the ancient Martian core dynamo [e.g., *Milbury et al.*, 2012], as well as on early tectonic activity. It is still under debate whether plate tectonics existed on early Mars [*Sleep*, 1994; *Connerney et al.*, 1999; *Harrison*, 2002; *Breuer and Spohn*, 2003; *Connerney et al.*, 2005], and the study of apparent polar wander and magnetization directions may help to answer this question. Also, paleopole positions have been used to argue for true polar wander on Mars [e.g., *Hood et al.*, 2005], which may have occurred due to the emplacement of the Tharsis bulge.

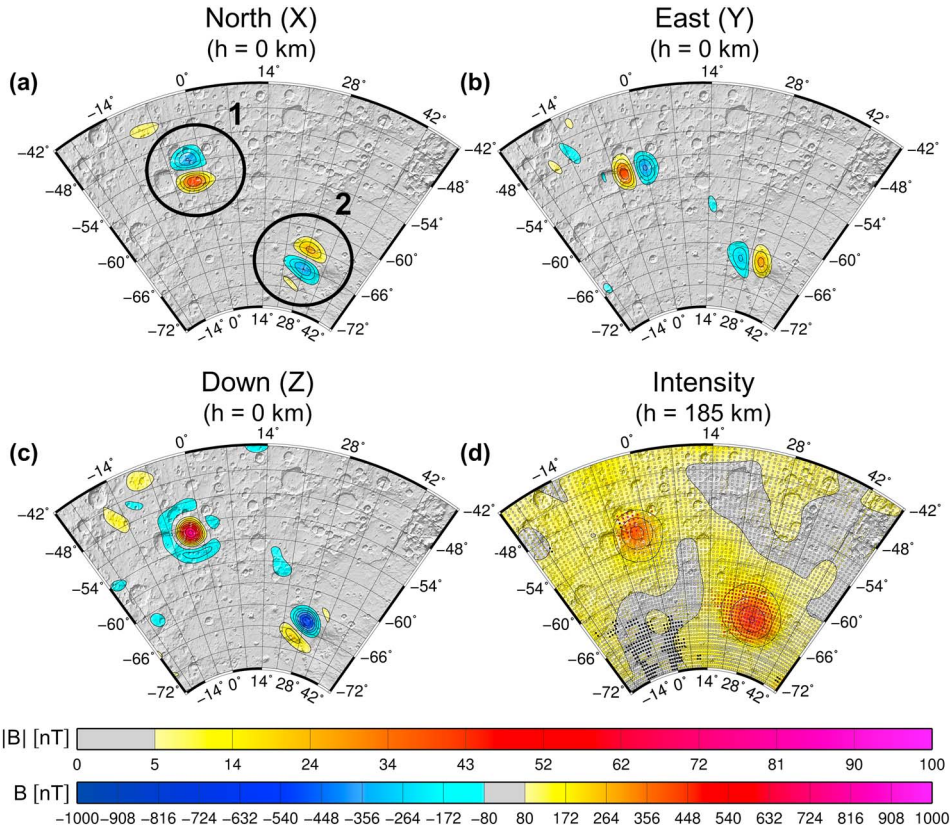

Figure 10. (a–c) Lithospheric field model at surface altitude showing the three magnetic field vector components of two isolated anomalies near the south pole. The color code of the magnetic field components is indicated by the lower color bar at the bottom of the figure. (d) Magnetic field intensity in the same area, but at 185 km altitude, with the color code of the field intensity shown in the upper color bar at the bottom of the figure. Electron Reflectometry (ER) data of *Lillis et al.* [2008a] are overlaid using color-coded circles and the same color bar, while black circles indicate regions of closed field lines where no ER data are available. The anomalies are clearly visible in the ER data as well.

Paleopole positions are usually estimated by fitting one or more homogeneously magnetized sources of a given shape and depth to the observed data. Ideally, the chosen anomalies should be isolated and/or correspond to geological features or gravitational anomalies. Using the presented model, two isolated anomalies near the south pole have been identified. These anomalies are presented in Figure 10, where all three magnetic field components are shown at surface altitude. The anomalies are centered at 357°E / 52°S (anomaly 1 in Figure 10a) and 28°E / 64°S (anomaly 2 in Figure 10a). Both anomalies exhibit a field signature corresponding to almost vertically oriented single dipoles, which hints at a uniform magnetization acquired at high magnetic latitudes in a global dipolar field. Interestingly, anomalies 1 and 2 are of opposite sign, indicating that magnetic reversals of the ancient Martian dynamo could have occurred [*Arkani-Hamed*, 2001b; *Frawley and Taylor*, 2004]. Alternatively, the magnetization of these anomalies may be due to a more complex geology, which cannot be resolved with this model. The intensity of the lithospheric field at 185 km altitude is shown in Figure 10d and compared to the Electron Reflectometer (ER) data (colored dots), which corresponds to the same altitude [*Lillis et al.*, 2008a]. Black circles in the ER data denote regions of closed crustal field lines, where no measurements were possible [*Lillis et al.*, 2008a]. The two anomalies are also observed in the ER data, with slightly stronger intensities as compared to our model. A spatial offset of ~100–150 km is present for anomaly 1, potentially due to tracing errors in the ER data, although these are expected to be lower [*Lillis et al.*, 2008a; R. Lillis, personal communication, 2013].

These anomalies may also be identified in other published models of the lithospheric field and anomaly 2 has already been mentioned by *Acuna et al.* [2001], but their detailed disvocery and interpretation has been hampered for two reasons: first, these anomalies are hardly visually detectable at the mapping phase orbit altitude, where many lithospheric field models have been evaluated. Second, these anomalies are relatively

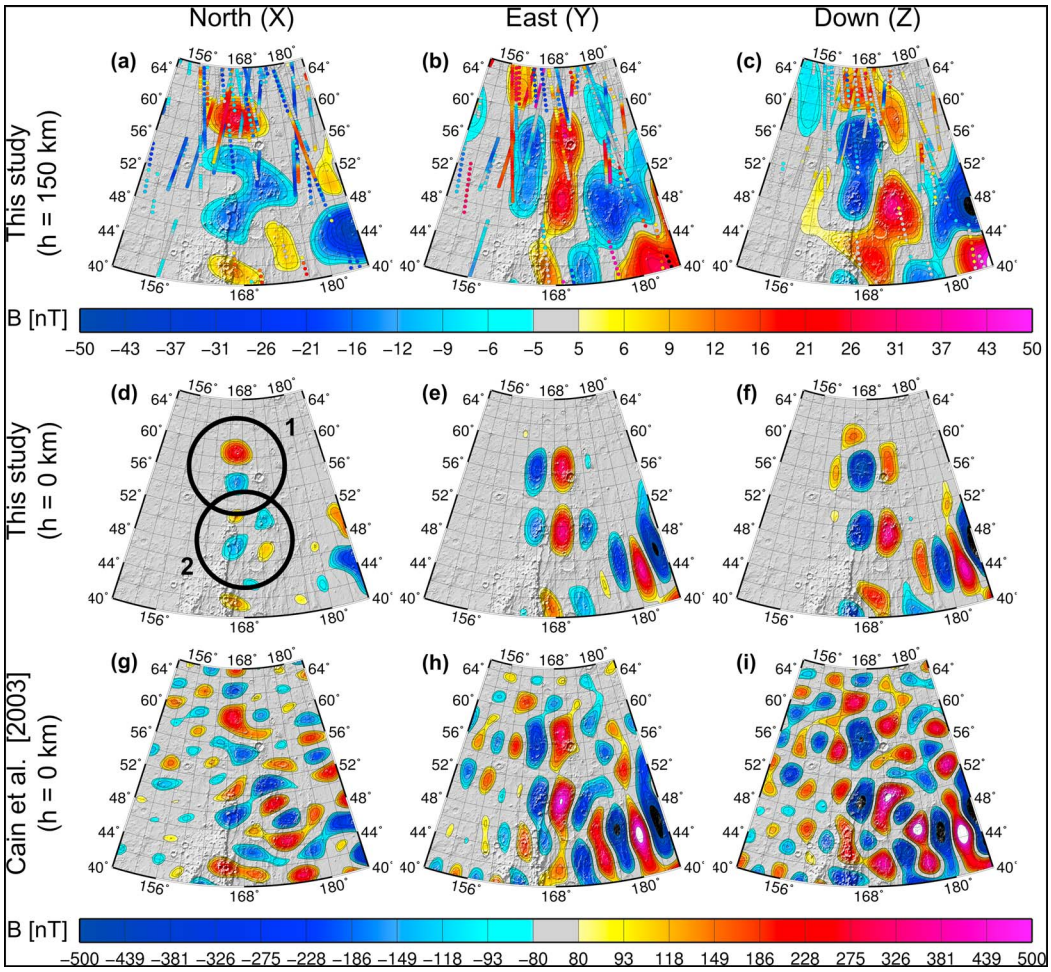

Figure 11. Maps of the lithospheric magnetic field near Arcadia Planitia showing isolated field anomalies (indicated by black circles labeled 1 and 2 in Figure 11d. (a–c) The horizontally north, east, and vertically down components of the presented lithospheric field model at 150 km altitude are shown. Colored circles indicate AB/SPO data tracks at altitudes between 120 and 180 km. (d–f) Same but at surface altitude without AB/SPO data tracks. (g–i) Same as Figures 11d–11f but for the model of *Cain et al.* [2003].

weak and can easily be masked by noise in the model. As the presented model is stable when downward continued to the surface, these anomalies now become visible even on a global map (cf. Figure 6).

Another two isolated anomalies are presented in Figure 11, and they are centered at 167°E / 57°N (anomaly 1 in Figure 11d) and 168°E / 49°N (anomaly 2 in Figure 11d) at the western rim of Arcadia Planitia in the northern lowlands. The anomalies are spaced approximately 450 km apart, and the predicted magnetic field for all three vector components is shown at 150 km altitude in Figures 11a–11c. For comparison, the AB/SPO data between 120 and 180 km altitude are also indicated by colored circles. At this altitude, the two anomalies are hardly separated and not easily recognized as such. Also, the field observed over these anomalies is influenced by the stronger anomalies located toward the southeast, which mask part of the signal. However, at surface altitude (Figures 11d–11f), the two anomalies are resolved. From a qualitative assessment, anomaly 1 most probably resembles that of an almost vertically oriented dipole, while anomaly 2 may either be horizontally oriented with a declination of around 60°, or be slightly inclined (~30°) with a declination of nearly 90°. This demonstrates that the downward continued field contains valuable information on the location and nature of these sources. For comparison, the downward continued field of the model of *Cain et al.* [2003] is shown in Figures 11g–11i, where the anomalies are difficult to identify due to most probably nonlithospheric field contributions to the model.

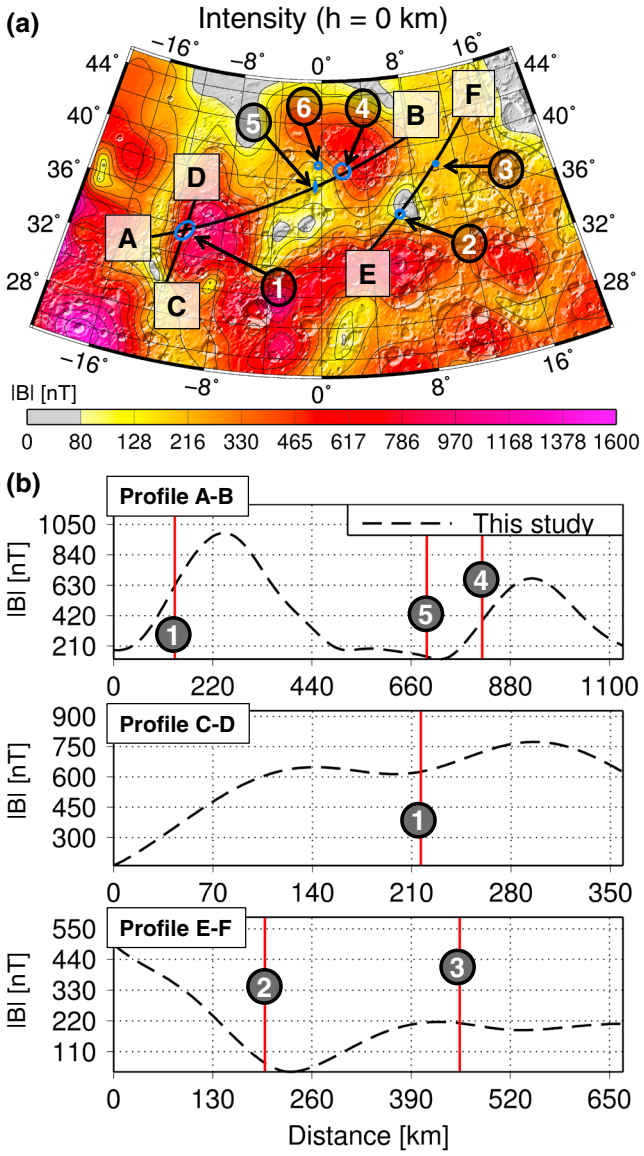

Figure 12. (a) Magnetic field intensity at surface altitude showing a recently discovered volcanic region over Arabia Terra [*Michalski and Bleacher*, 2013]. The volcanoes in this region are characterized by calderas without an associated volcanic cone and are marked by blue ellipses. The most prominent features in this area include Eden Patera (labeled 1) and Euphrates Patera (labeled 3), while a distinct magnetic anomaly was identified at Siloe Patera (labeled 2). Other visible calderas include Ismenia Patera (labeled 4), Oxus Cavus (labeled 5), and Oxus Patera (labeled 6) (b) Magnetic field intensity along the profiles shown in Figure 12a (black line and letters). The position of the respective volcanic calderas is indicated by vertical red lines and the respective numeric labels.

4.7. Magnetic Signature of Volcanoes

Volcanic activity is associated with elevated temperatures and can be responsible for thermoremanent magnetization or thermal demagnetization if the Curie temperature of the magnetic minerals is exceeded [*Johnson and Phillips*, 2005; *Lillis et al.*, 2006]. The interpretation of magnetic signatures can therefore potentially constrain the history of the Martian core dynamo. However, *Lillis et al.* [2013] pointed out that using magnetic anomalies associated with volcanic features is subject to some significant caveats: first, the magnetization of a large volume of crust must be changed at approximately the same time, requiring very large magma chambers, sills, and dikes. Second, the surface age does not necessarily correspond to the age of the (de)magnetization event, as intrusions may play an important role and a larger, earlier event could be covered by later activity. Nevertheless, magnetic signatures associated with volcanoes have been used to constrain the lifetime of the Martian core dynamo [*Lillis et al.*, 2006; *Milbury et al.*, 2012] or to determine paleopole locations [*Langlais and Purucker*, 2007; *Hood et al.*, 2010]. The latter approach is particularly promising as the source of the associated anomaly is relatively well known in this case. In addition, the magnetic signature of volcanoes has been used to constrain the volume of magma chambers and thus the ratio of intrusive to extrusive volcanism [*Lillis et al.*, 2008a, 2009].

Recently, a previously undetected volcanic province has been identified in Arabia Terra, which consists of several volcanic calderas [*Michalski and Bleacher*, 2013]. The corresponding region and magnetic field intensity at surface altitude are shown in Figure 12a, where the volcanic calderas are marked by blue ellipses. The calderas can easily be mistaken for degraded impact craters, and *Michalski and Bleacher* [2013] note that Eden Patera and Euphrates Patera (labeled 1 and 3 in Figure 12, respectively) show the most unambiguous signs of volcanic activity. Eden Patera is located at the rim of a positive magnetic anomaly (cf. Figure 12a and profile A-B in Figure 12b), but no clear signature of (de)magnetization appears to be associated with it, although the profile along C-D suggests a slightly weaker field above the caldera. Euphrates Patera appears not to be associated with any distinct anomaly (label 3 and profile E-F in Figure 12), either because its magnetic signal cannot be resolved, or because its

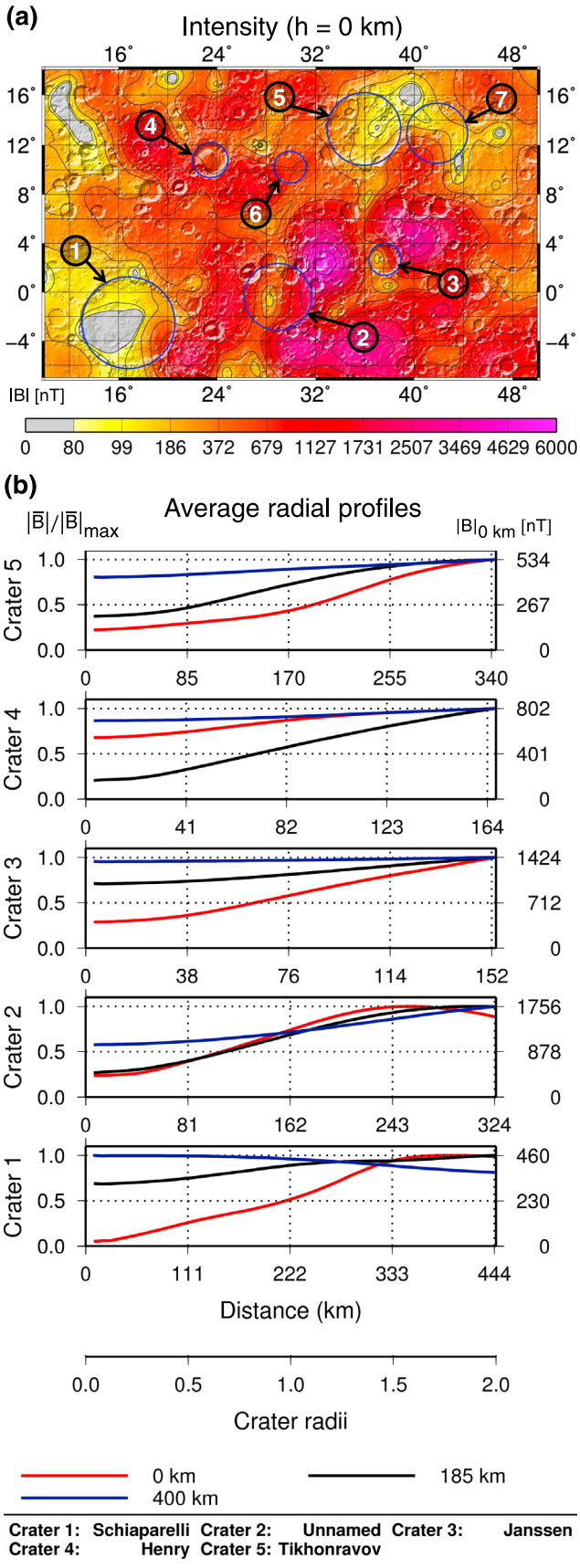

main magma chamber was not located directly underneath the caldera. In this case, an analysis of the gravity data would provide further insight. Siloe Patera (labeled 2 in Figure 12) is another caldera within this province which is probably of volcanic origin and is associated with a region of low field intensity (cf. profile E-F in Figure 12b). This suggests that the core dynamo was probably extinct when this structure was still active. The ages of Siloe Patera and the other volcanic features in this region have not been determined yet, but *Michalski and Bleacher* [2013] suggest that they were formed in the Late Noachian to Early Hesperian period, and a more detailed analysis of the ages of these features would provide important information on the magnetic history of Mars. Two other features of likely volcanic origin are Ismenia Patera and Oxus Cavus (labeled 4 and 5 in Figure 12, respectively). Ismenia Patera is located at the rim of a larger positive anomaly, and the situation is similar to Eden Patera. Oxus Cavus,

Figure 13. (a) Magnetic field intensity evaluated at the mean planetary radius over a region of 2350 × 1500 km located within the southern part of Arabia Terra. Impact craters with a diameter larger than 150 km are shown by blue ellipses. These include Schiaparelli (446 km in diameter, labeled 1 in Figure 13a), an unnamed crater (326 km in diameter, labeled 2 in Figure 13a), Janssen (154 km in diameter, labeled 3 in Figure 13a), Henry (168 km in diameter, labeled 4 in Figure 13a), Tikhonravov (344 km in diameter, labeled 5 in Figure 13a), Arago crater (152 km in diameter, labeled 6 in Figure 13a) and another unnamed crater (285 km in diameter, labeled 7 in Figure 13a). (b) Circumferential average of the magnetic field intensity as a function of the radial distance from the crater's center and for altitudes of 400 km (blue solid line), 185 km (black line), and at the mean planetary radius (red line). The normalized averaged intensity and the intensity at the mean planetary radius are given on the left and right ordinate, respectively. The shown circumferentially averaged profiles correspond to the labeled impact craters in Figure 13a, for which a related magnetic signature can be observed.

on the other hand, is located on a local magnetic field minimum (cf. profile A-B in Figure 12b) in a region of low-field intensity, and may have partially demagnetized the crust.

4.8. Magnetic Signature of Impact Craters

Planetary impacts are capable of changing the magnetic signature of the crust through shock and thermal (de)magnetization, and they can simultaneously reset the surface age and the magnetization within a large crustal volume. Therefore, they can potentially be used to constrain the lifetime of the Martian dynamo, and the four largest impact basins on Mars appear largely demagnetized (cf. Figure 6), supporting the conclusion that Mars' core dynamo was extinct ~4 Gyr ago. The magnetic signature of smaller (< 1000 km in diameter) craters is more difficult to assess, as information on their magnetization cannot directly be extracted from data gathered at the MGS mapping phase orbit altitude [*Lillis et al.*, 2010]. To circumvent this problem, *Lillis et al.* [2013] have used a statistical approach to investigate the magnetic signature of craters down to 300 km in diameter, and we will show here that the presented model is also capable of resolving the magnetic signature of small craters when it is downward continued to surface altitude. In this case, the diameter of the smallest crater for which a magnetic signature can be observed is limited by the resolution of the model, corresponding to ~190 km.

In Figure 13a, the magnetic field intensity at surface altitude is shown for a 2350 × 1500 km large region within the southern part of Arabia Terra. Several impact craters with a diameter larger than 150 km are present in the area, including Schiaparelli (446 km in diameter, labeled 1 in Figure 13a), an unnamed crater (326 km in diameter, labeled 2 in Figure 13a), Janssen (154 km in diameter, labeled 3 in Figure 13a), Henry (168 km in diameter, labeled 4 in Figure 13a), and Tikhonravov (344 km in diameter, labeled 5 in Figure 13a). All of these craters appear to be at least partially demagnetized, whereas no distinct anomaly can be associated with Arago crater (152 km in diameter, labeled 6 in Figure 13a) and an unnamed crater (285 km in diameter, labeled 7 in Figure 13a). The normalized circumferential averages of magnetic field intensity above the former craters as a function of radial distance from the crater's center are shown in Figure 13b for altitudes of 400 km (blue solid line), 185 km (black solid line), and at the surface (red solid line). Schiaparelli crater (labelled 1 here) was previously investigated by *Lillis et al.* [2013], who performed a statistical analysis on the expected and observed magnetic fields at 185 km altitude and they argue that Schiaparelli is likely magnetized. The circumferentially averaged magnetic profile in Figure 13b (Crater 1) indicates that the signal at 185 km altitude indeed suggests that Schiaparelli is not completely demagnetized, but the presented model at lower altitudes reveals a near-zero field region to be directly associated with the crater (cf. Figure 13a), and the respective profile shows a large contrast of magnetic fields inside and outside the crater (cf. Figure 13b). This would be in accordance with the early dynamo shutdown hypothesis, as Schiaparelli's age is estimated to be approximately 3.92 Ga [*Werner*, 2008], although the crater might be significantly older [*Lillis et al.*, 2013]. The unnamed crater labeled 2 appears to be at least partially demagnetized, and the profiles at 185 km and 0 km altitude are very similar, which may be due to larger coherence wavelengths as compared to Schiaparelli. The diameter of Jannsen crater (154 km in diameter, labeled 3 in Figure 13a) is at the resolution limit of the presented model, and the magnetic signature becomes more distinct with decreasing altitude, confirming the ability of the presented model to resolve the magnetic signature associated with such small craters. The field over Henry crater (168 km in diameter, labeled 4 in Figure 13a) shows a relatively low averaged field within the crater at an altitude of 185 km, resembling the signature of a demagnetized crater, but the field contrast is much less pronounced for altitudes of 0 and 400 km, and the crater is probably not fully demagnetized. This example shows that the characteristics of the magnetic signature of impact craters can change in a various ways with altitude, especially as the observed field at different altitudes depends on crater size and the coherence wavelength of crustal magnetization. Finally, the magnetic field profile for Tikhonravov Crater, which is estimated to be 4.10 Ga. old [*Werner*, 2008], shows a low averaged field within the crater, with relative amplitudes decreasing for lower altitudes, suggesting that it is rather demagnetized. This is in contrast to the results by *Lillis et al.* [2013], who found Tikhonravov to be at least partially magnetized.

A low-field region in Terra Sirenum, centered at 42°S and 195°E, is shown in Figure 14 for altitudes of 0 km (a) and 185 km (b), and the map is overlaid with ER data [*Lillis et al.*, 2008a] for the latter. Black circles in the ER data denote regions of closed crustal field lines, where no measurements were possible [*Lillis et al.*, 2008a]. Again, the ER data agree well with our model, with the low-field region being slightly more pronounced in the ER data. The region is situated between Newton and Copernicus craters, and possibly associated with a quasi-circular depression and related circular thin area (indicated by the blue circle in Figure 14) as identified

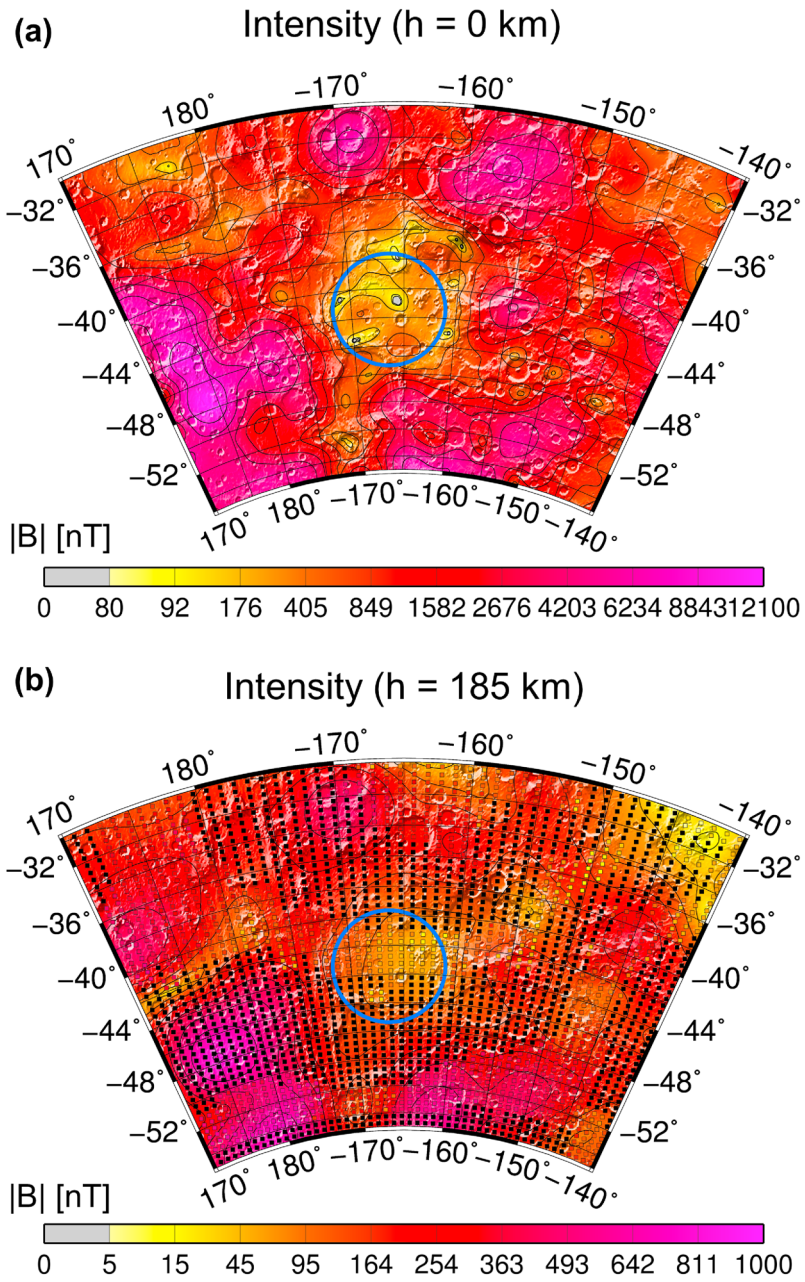

Figure 14. (a) Modeled magnetic field intensity at surface altitude in Terra Sirenum. A low-field region is centered at 42° S and 195° E. (b) Same region but with the magnetic field evaluated at 185 km altitude. Electron Reflectometry (ER) data of *Lillis et al.* [2008a] are overlaid using color-coded circles and the same color bar, while black circles indicate regions of closed field lines where no ER data are available. The low-field region is also visible at this altitude and is confirmed by the ER data. A possible buried impact crater is indicated by the blue circle [*Langlais et al.*, 2004; *Edgar and Frey*, 2008].

by *Edgar and Frey* [2008, Figure 3]. This potentially buried crater has also been discussed by *Langlais et al.* [2004] (called Sirenum there), but they do not explicitly comment on its magnetization.

5. Summary and Conclusions

We have presented a spherical harmonic (SH) model of the lithospheric magnetic field of Mars, which is expanded up to SH degree and order 110. It is the first model to be based on the entire Mars Global Surveyor data set, using nighttime data of the stable mapping phase orbit at 400 km altitude and low-altitude AB/SPO daytime and nighttime data. The data were thoroughly analyzed to derive a priori MPO data weights and

to identify erroneous AB/SPO tracks. Also, as nonlithospheric field contributions were found to be present in all data sets, external fields for the dayside and nightside were coestimated. Remaining data outliers and incompatible data points in the MPO data set were handled by using a modified Huber-Norm. This has the advantage that spurious data does not have to be removed a priori but can be handled during inversion.

In contrast to equivalent source dipole models, spherical harmonic models can directly be downward continued to the planetary surface. However, when interpreting the obtained map, it should be kept in mind that the resolution is limited by the maximum SH degree and the actual field might contain considerably more small-scale structure. Also, it is difficult to distinguish between anomalies of lithospheric and nonlithospheric origin and noise can sensibly influence the predicted field at low altitudes. The latter will lead to unrealistically strong oscillations of the model field at surface altitude, which masks the lithospheric part of the field (cf. Figure 9). Hence, careful regularization is important to obtain a stable map below orbit altitude, and the right balance between suppressing part of the lithospheric signal and noise must be found. The presented model was regularized using an IRLS algorithm which approaches a L1 measure of model complexity. This is based on the observation that strong localized gradients are present on Mars, and the distribution of horizontal magnetic field gradients may rather follow a Laplacian than a Gaussian distribution. The L1 regularization was applied in physical space and therefore allows the solution to maintain sharp field gradients, while at the same time effectively suppressing noise, leading to a robust model which can be downward continued to the surface.

The quality of the model was investigated through an analysis of the statistics and spatial distribution of the residuals from the model to the data. The weighted residuals to the MPO data show a fairly homogeneous distribution, with only minor large-scale structures visible for the horizontal components (cf. Figure 7). For the AB/SPO data, on the other hand, small-scale structures are visible, especially over regions of high field intensity. This indicates that a higher SH degree than 110 may be justified and SH degrees below 90 are definitely too low to represent the AB/SPO data (cf. Figure 3). However, significant nonlithospheric field contributions are present in the AB/SPO daytime data, and a higher SH expansion degree might well increase the influence of nonlithospheric signals in the model.

The resulting magnetic field map reproduces the known features of the Martian magnetic field such as very weak fields over the largest impact basins and volcanic provinces. Also, the strongest fields are observed over Terra Cimmeria and Terra Sirenum, with maximum fields of −11900/+10800 nT for the vertically down component, and −6600/+5200 nT and −8500/+9800 nT for the horizontally east and north components, respectively. On the other hand, the northern lowlands are largely devoid of strong fields.

Overall, the presented model provides a high-resolution map of the Martian lithospheric magnetic field observed at satellite altitude, which is robust when downward continued to the surface. Due to these properties, the model is an important tool for addressing many of the unresolved questions related to the history of the Martian magnetic field. The model can resolve weak isolated magnetic anomalies, which can be studied to determine paleopole positions and rock magnetization. Furthermore, the magnetic signature of impact craters with diameters down to 190 km can be resolved, and the work of *Lillis et al.* [2013] may be expanded to craters of smaller size, further improving our knowledge of the Martian magnetic field history.

Some remarkable features which have been identified with the new model include two isolated anomalies near the south pole (cf. Figure 10), as well as a low-field region situated within the strong magnetic anomalies of Terra Sirenum (cf. Figure 14), which may be associated with an old, buried impact crater [*Langlais et al.*, 2004; *Edgar and Frey*, 2008]. In addition, the magnetic field signature of a recently discovered field of ancient supervolcanoes [*Michalski and Bleacher*, 2013] in Arabia Terra has been described (cf. Figure 12), and a local field minimum associated with Siloe Patera, which most probably formed during the Late Noachian / Early Hesperian periods, has been presented.

The spherical harmonic coefficients of the presented model, maps of the modeled external fields at an altitude of 400 km, as well as maps of the modeled internal magnetic field at altitudes of 0, 185, and 400 km are provided with the supporting information. However, it should be kept in mind that the maximum resolution of the model is limited by the truncation of the SH model at degree and order 110, corresponding to a minimum resolvable wavelength of roughly 190 km at surface altitude.

Acknowledgments
We would like to thank Benoit Langlais and one anonymous reviewer for their comments and suggestions, which helped to improve the original manuscript. Most maps and plots of this article were produced with GMT [*Wessel and Smith*, 1991]. The MGS magnetometer data were obtained from the Planetary Plasma Interactions Node of the Planetary Data System (http://ppi.pds.nasa.gov/). The work was funded by the German Research Association within the "Schwerpunktprojekt 1488-Planetary Magnetism" under grants GR3751/1-1 (A.M. and M.G.) and LE2477/3-1 (V.L.).

References

Acuña, M. H., et al. (1998), Magnetic field and plasma observations at Mars: Initial results of the Mars Global Surveyor Mission, *Science*, *279*(5357), 1676–1680, doi:10.1126/science.279.5357.1676.

Acuña, M. H., et al. (1999), Global distribution of crustal magnetization discovered by the Mars Global Surveyor MAG/ER Experiment, *Science*, *284*(5415), 790–793, doi:10.1126/science.284.5415.790.

Acuña, M. H., et al. (2001), Magnetic field of Mars: Summary of results from the aerobraking and mapping orbits, *J. Geophys. Res.*, *106*(E10), 23,403–23,417, doi:10.1029/2000JE001404.

Albee, A. L., R. E. Arvidson, F. Palluconi, and T. Thorpe (2001), Overview of the Mars Global Surveyor mission, *J. Geophys. Res.*, *106*(E10), 23,291–23,316, doi:10.1029/2000JE001306.

Amit, H., U. R. Christensen, and B. Langlais (2011), The influence of degree-1 mantle heterogeneity on the past dynamo of Mars, *Phys. Earth Planet. Inter.*, *189*(1–2), 63–79, doi:10.1016/j.pepi.2011.07.008.

Arkani-Hamed, J. (2001a), A 50-degree spherical harmonic model of the magnetic field of Mars, *J. Geophys. Res.*, *106*(E10), 23,197–23,208, doi:10.1029/2000JE001365.

Arkani-Hamed, J. (2001b), Paleomagnetic pole positions and pole reversals of Mars, *Geophys. Res. Lett.*, *28*(17), 3409–3412, doi:10.1029/2001GL012928.

Arkani-Hamed, J. (2002a), Magnetization of the Martian crust, *J. Geophys. Res.*, *107*(E5), 5032, doi:10.1029/2001JE001496.

Arkani-Hamed, J. (2002b), An improved 50-degree spherical harmonic model of the magnetic field of Mars derived from both high-altitude and low-altitude data, *J. Geophys. Res.*, *107*(E10), 5083, doi:10.1029/2001JE001835.

Arkani-Hamed, J. (2004a), A coherent model of the crustal magnetic field of Mars, *J. Geophys. Res.*, *109*, E09005, doi:10.1029/2004JE002265.

Arkani-Hamed, J. (2004b), Timing of the Martian core dynamo, *J. Geophys. Res.*, *109*, E03006, doi:10.1029/2003JE002195.

Arkani-Hamed, J., and D. Boutin (2012), Is the primordial crust of Mars magnetized?, *Icarus*, *221*(1), 192–207, doi:10.1016/j.icarus.2012.07.030.

Aster, R., B. Borchers, and C. Thurber (2012), *Parameter Estimation and Inverse Problems*, 2nd ed., Elsevier Academic Press, Amsterdam.

Brain, D. A., F. Bagenal, M. H. Acuña, and J. E. P. Connerney (2003), Martian magnetic morphology: Contributions from the solar wind and crust, *J. Geophys. Res.*, *108*(A12), 1424, doi:10.1029/2002JA009482.

Breuer, D., and T. Spohn (2003), Early plate tectonics versus single-plate tectonics on Mars: Evidence from magnetic field history and crust evolution, *J. Geophys. Res.*, *108*(E7), 5072, doi:10.1029/2002JE001999.

Cain, J. C., B. B. Ferguson, and D. Mozzoni (2003), An $n = 90$ internal potential function of the Martian crustal magnetic field, *J. Geophys. Res.*, *108*(E2), 5008, doi:10.1029/2000JE001487.

Chassefière, E., B. Langlais, Y. Quesnel, and F. Leblanc (2013), The fate of early Mars' lost water: The role of serpentinization, *J. Geophys. Res. Planets*, *118*(5), 1123–1134, doi:10.1002/jgre.20089.

Chiao, L.-Y., J.-R. Lin, and Y.-C. Gung (2006), Crustal magnetization equivalent source model of Mars constructed from a hierarchical multiresolution inversion of the Mars Global Surveyor data, *J. Geophys. Res.*, *111*, E12010, doi:10.1029/2006JE002725.

Citron, R. I., and S. Zhong (2012), Constraints on the formation of the Martian crustal dichotomy from remnant crustal magnetism, *Phys. Earth Planet. Inter.*, *212*, 55–63, doi:10.1016/j.pepi.2012.09.008.

Connerney, J. E. P., M. H. Acuna, P. J. Wasilewski, N. F. Ness, H. Rème, C. Mazelle, D. Vignes, R. P. Lin, D. L. Mitchell, and P. A. Cloutier (1999), Magnetic lineations in the ancient crust of Mars, *Science*, *284*(5415), 794–798, doi:10.1126/science.284.5415.794.

Connerney, J. E. P., M. H. Acuña, N. F. Ness, G. Kletetschka, D. L. Mitchell, R. P. Lin, and H. Rème (2005), Tectonic implications of Mars crustal magnetism, *Proc. Natl. Acad. Sci.*, *102*(42), 14,970–14,975, doi:10.1073/pnas.0507469102.

Dietrich, W., and J. Wicht (2013), A hemispherical dynamo model: Implications for the Martian crustal magnetization, *Phys. Earth Planet. Inter.*, *217*, 10–21, doi:10.1016/j.pepi.2013.01.001.

Echer, E., W. D. Gonzalez, B. T. Tsurutani, and A. L. C. Gonzalez (2008), Interplanetary conditions causing intense geomagnetic storms ($Dst \leq -100$ nT) during solar cycle 23 (1996–2006), *J. Geophys. Res.*, *113*, A05221, doi:10.1029/2007JA012744.

Echer, E., B. T. Tsurutani, and W. D. Gonzalez (2013), Interplanetary origins of moderate (-100 nT $< Dst \leq -50$ nT) geomagnetic storms during solar cycle 23 (1996–2008), *J. Geophys. Res. Space Physics*, *118*(1), 385–392, doi:10.1029/2012JA018086.

Edgar, L. A., and H. V. Frey (2008), Buried impact basin distribution on Mars: Contributions from crustal thickness data, *Geophys. Res. Lett.*, *35*, L02201, doi:10.1029/2007GL031466.

Farquharson, C. G., and D. W. Oldenburg (1998), Non-linear inversion using general measures of data misfit and model structure, *Geophys. J. Int.*, *134*, 213–227, doi:10.1046/j.1365-246x.1998.00555.x.

Ferguson, B. B., J. C. Cain, D. H. Crider, D. A. Brain, and E. M. Harnett (2005), External fields on the nightside of Mars at Mars Global Surveyor mapping altitudes, *Geophys. Res. Lett.*, *32*, L16105, doi:10.1029/2004GL021964.

Frawley, J. J., and P. T. Taylor (2004), Paleo-pole positions from Martian magnetic anomaly data, *Icarus*, *172*(2), 316–327, doi:10.1016/j.icarus.2004.07.025.

Gubbins, D., D. Ivers, S. M. Masterton, and D. E. Winch (2011), Analysis of lithospheric magnetization in vector spherical harmonics, *Geophys. J. Int.*, *187*(1), 99–117, doi:10.1111/j.1365-246X.2011.05153.x.

Halekas, J. S., D. A. Brain, R. J. Lillis, M. O. Fillingim, D. L. Mitchell, and R. P. Lin (2006), Current sheets at low altitudes in the Martian magnetotail, *Geophys. Res. Lett.*, *33*, L13101, doi:10.1029/2006GL026229.

Harrison, C. G. A. (2002), Questions about magnetic lineations in the ancient crust of Mars, *Science*, *287*(5453), 547, doi:10.1126/science.287.5453.547a.

Hood, L. L., and A. Zakharian (2001), Mapping and modeling of magnetic anomalies in the northern polar region of Mars, *J. Geophys. Res.*, *106*(E7), 14,601–14,619, doi:10.1029/2000JE001304.

Hood, L. L., C. N. Young, N. C. Richmond, and K. P. Harrison (2005), Modeling of major Martian magnetic anomalies: Further evidence for polar reorientations during the Noachian, *Icarus*, *177*(1), 144–173, doi:10.1016/j.icarus.2005.02.008.

Hood, L. L., K. P. Harrison, B. Langlais, R. J. Lillis, F. Poulet, and D. A. Williams (2010), Magnetic anomalies near Apollinaris Patera and the Medusae Fossae Formation in Lucus Planum, Mars, *Icarus*, *208*(1), 118–131, doi:10.1016/j.icarus.2010.01.009.

Huber, P. J. (1964), Robust estimation of a location parameter, *Ann. Math. Stat.*, *35*(1), 73–101, doi:10.1214/aoms/1177703732.

Johnson, C. L., and R. J. Phillips (2005), Evolution of the Tharsis region of Mars: Insights from magnetic field observations, *Earth Planet. Sci. Lett.*, *230*(3–4), 241–254, doi:10.1016/j.epsl.2004.10.038.

Langlais, B., and M. Purucker (2007), A polar magnetic paleopole associated with Apollinaris Patera, Mars, *Planet. Space Sci.*, *55*(3), 270–279, doi:10.1016/j.pss.2006.03.008.

Langlais, B., M. E. Purucker, and M. Mandea (2004), Crustal magnetic field of Mars, *J. Geophys. Res.*, *109*, E02008, doi:10.1029/2003JE002048.

Langlais, B., R. J. Lillis, and M. Purucker (2010), An improved model of the magnetic lithospheric field of Mars using both MGS-MAG and MGS-ER measurements, paper presented at European Planetary Science Congress 2010, vol. 5, EPSC2010-393, Rome, Italy, 20–24 Sept.
Lesur, V. (2006), Introducing localized constraints in global geomagnetic field modelling, *Earth Planets Space*, *58*(4), 477–483.
Lesur, V., and A. Jackson (2000), Exact solutions for internally induced magnetization in a shell, *Geophys. J. Int.*, *140*(2), 453–459, doi:10.1046/j.1365-246X.2000.00046.x.
Lesur, V., M. Rother, F. Vervelidou, M. Hamoudi, and E. Thébault (2013), Post-processing scheme for modelling the lithospheric magnetic field, *Solid Earth*, *4*, 105–118, doi:10.5194/se-4-105-2013.
Lillis, R. J., D. L. Mitchell, R. P. Lin, J. E. P. Connerney, and M. H. Acuña (2004), Mapping crustal magnetic fields at Mars using electron reflectometry, *Geophys. Res. Lett.*, *31*, L15702, doi:10.1029/2004GL020189.
Lillis, R. J., M. Manga, D. L. Mitchell, R. P. Lin, and M. H. Acuña (2006), Unusual magnetic signature of the Hadriaca Patera Volcano: Implications for early Mars, *Geophys. Res. Lett.*, *33*, L03202, doi:10.1029/2005GL024905.
Lillis, R. J., H. V. Frey, M. Manga, D. L. Mitchell, R. P. Lin, M. H. Acuña, and S. W. Bougher (2008a), An improved crustal magnetic field map of Mars from electron reflectometry: Highland volcano magmatic history and the end of the Martian dynamo, *Icarus*, *194*(2), 575–596, doi:10.1016/j.icarus.2007.09.032.
Lillis, R. J., H. V. Frey, and M. Manga (2008b), Rapid decrease in Martian crustal magnetization in the Noachian era: Implications for the dynamo and climate of early Mars, *Geophys. Res. Lett.*, *35*, L14203, doi:10.1029/2008GL034338.
Lillis, R. J., D. L. Mitchell, R. P. Lin, and M. H. Acuña (2008c), Electron reflectometry in the Martian atmosphere, *Icarus*, *194*(2), 544–561, doi:10.1016/j.icarus.2007.09.030.
Lillis, R. J., J. Dufek, J. E. Bleacher, and M. Manga (2009), Demagnetization of crust by magmatic intrusion near the Arsia Mons volcano: Magnetic and thermal implications for the development of the Tharsis province, Mars, *J. Volcanol. Geotherm. Res.*, *185*(1–2), 123–138, doi:10.1016/j.jvolgeores.2008.12.007.
Lillis, R. J., M. E. Purucker, J. S. Halekas, K. L. Louzada, S. T. Stewart-Mukhopadhyay, M. Manga, and H. V. Frey (2010), Study of impact demagnetization at Mars using Monte Carlo modeling and multiple altitude data, *J. Geophys. Res.*, *115*, E07007, doi:10.1029/2009JE003556.
Lillis, R. J., S. T. Stewart, and M. Manga (2013), Demagnetization by basin-forming impacts on early Mars: Contributions from shock, heat, and excavation, *J. Geophys. Res. Planets*, *118*(5), 1045–1062, doi:10.1002/jgre.20085.
Lowes, F. J. (1966), Mean-square values on sphere of spherical harmonic vector fields, *J. Geophys. Res.*, *71*(8), 2179, doi:10.1029/JZ071i008p02179.
Luhmann, J. G., and L. H. Brace (1991), Near-Mars space, *Rev. Geophys.*, *29*(2), 121–140, doi:10.1029/91RG00066.
Mauersberger, P. (1956), Das Mittel der Energiedichte des geomagnetischen Hauptfeldes an der Erdoberfläche und seine säkulare Änderung, *Gerlands Beitr. Geophys.*, *65*, 207–215.
Michalski, J. R., and J. E. Bleacher (2013), Supervolcanoes within an ancient volcanic province in Arabia Terra, Mars, *Nature*, *502*, 47–52, doi:10.1038/nature12482.
Milbury, C., and G. Schubert (2010), Search for the global signature of the Martian dynamo, *J. Geophys. Res.*, *115*, E10010, doi:10.1029/2010JE003617.
Milbury, C., G. Schubert, C. A. Raymond, S. E. Smrekar, and B. Langlais (2012), The history of Mars' dynamo as revealed by modeling magnetic anomalies near Tyrrhenus Mons and Syrtis Major, *J. Geophys. Res.*, *117*, E10007, doi:10.1029/2012JE004099.
Mitchell, D. L., R. P. Lin, C. Mazelle, H. Rème, P. A. Cloutier, J. E. P. Connerney, M. H. Acuña, and N. F. Ness (2001), Probing Mars' crustal magnetic field and ionosphere with the MGS Electron Reflectometer, *J. Geophys. Res.*, *106*(E10), 23,419–23,428, doi:10.1029/2000JE001435.
Mohit, P. S., and J. Arkani-Hamed (2004), Impact demagnetization of the Martian crust, *Icarus*, *168*(2), 305–317, doi:10.1016/j.icarus.2003.12.005.
Olsen, N., K.-H. Glassmeier, and X. Jia (2010), Separation of the magnetic field into external and internal parts, *Space Sci. Rev.*, *152*(1–4), 135–157, doi:10.1007/s11214-009-9563-0.
Parker, R. L. (1994), *Geophysical Inverse Problems*, 1st ed., Princeton Univ. Press, Princeton, N. J.
Parker, R. L., L. Shure, and J. A. Hildebrand (1987), The application of inverse theory to seamount magnetism, *Rev. Geophys.*, *25*(1), 17–40, doi:10.1029/RG025i001p00017.
Purucker, M., D. Ravat, H. Frey, C. Voorhies, T. Sabaka, and M. Acuña (2000), An altitude-normalized magnetic map of Mars and its interpretation, *Geophys. Res. Lett.*, *27*(16), 2449–2452, doi:10.1029/2000GL000072.
Quesnel, Y., C. Sotin, B. Langlais, S. Costin, M. Mandea, M. Gottschalk, and J. Dyment (2009), Serpentinization of the Martian crust during Noachian, *Earth Planet. Sci. Lett.*, *277*(1–2), 184–193, doi:10.1016/j.epsl.2008.10.012.
Runcorn, S. K. (1975), On the interpretation of lunar magnetism, *Phys. Earth Planet. Inter.*, *10*(4), 327–225, doi:10.1016/0031-9201(75)90059-X.
Schmitz, D. R., and J. C. Cain (1983), Geomagnetic spherical harmonic analyses: 1. Techniques, *J. Geophys. Res.*, *88*(B2), 1222–1228, doi:10.1029/JB088iB02p01222.
Schubert, G., C. T. Russell, and W. B. Moore (2000), Geophysics: Timing of the Martian dynamo, *Nature*, *408*, 666–667, doi:10.1038/35047163.
Shure, L., R. L. Parker, and G. E. Backus (1982), Harmonic splines for geomagnetic modelling, *Phys. Earth Planet. Inter.*, *28*(3), 215–229, doi:10.1016/0031-9201(82)90003-6.
Sleep, N. H. (1994), Martian plate tectonics, *J. Geophys. Res.*, *99*(E3), 5639–5655, doi:10.1029/94JE00216.
Stanley, S. L., M. T. Elkins-Tanton, M. T. Zuber, and E. M. Parmentier (2008), Mars' paleomagnetic field as the result of a single-hemisphere dynamo, *Science*, *321*(5897), 1822–1825, doi:10.1126/science.1161119.
Stevenson, D. J. (2001), Mars' core and magnetism, *Nature*, *412*, 214–219, doi:10.1038/35084155.
Voorhies, C. V., T. J. Sabaka, and M. Purucker (2002), On magnetic spectra of Earth and Mars, *J. Geophys. Res.*, *107*(E6), 5034, doi:10.1029/2001JE001534.
Werner, S. C. (2008), The early Martian evolution—Constraints from basin formation ages, *Icarus*, *195*(1), 45–60, doi:10.1016/j.icarus.2007.12.008.
Wessel, P., and W. H. F. Smith (1991), Free software helps map and display data, *Eos Trans. AGU*, *72*(41), 441–446, doi:10.1029/90EO00319.
Whaler, K. A., and M. E. Purucker (2005), A spatially continuous magnetization model for Mars, *J. Geophys. Res.*, *110*, E09001, doi:10.1029/2004JE002393.